

1 **Deciphering earthquake triggering mechanisms for**
2 **induced seismicity using a fully coupled poroelastic**
3 **model and machine learning analysis**

4 **R. G. Hill^{1,2}, D. Trugman³, and M. Weingarten¹**

5 ¹Department of Geological Sciences, San Diego State University, San Diego, California

6 ²Scripps Institution of Oceanography, University of California San Diego, La Jolla, California

7 ³Nevada Seismological Laboratory, University of Nevada, Reno, Nevada

8 **Key Points:**

- 9 • Combining physics-based and machine learning models can decipher earthquake
10 triggering mechanisms for induced seismicity.
- 11 • Injection-driven earthquakes account for just $22\pm 5\%$ of all earthquakes in the Para-
12 dox Valley catalog.
- 13 • Injection-driven earthquakes have a larger b-value, are closer to the well, and oc-
14 cur earlier in the injection history.

Corresponding author: Ryley G. Hill, ryleyghill@gmail.com

Abstract

In areas of induced seismicity, earthquakes can be triggered by stress changes from fluid injection and from static deformation caused by fault slip. Here we present a method to distinguish between injection-driven and earthquake-driven triggering of induced seismicity by combining a calibrated, fully-coupled, poroelastic stress model of wastewater injection with a random forest machine learning algorithm trained on both earthquake catalog and modeled stress features. We investigate the classic Paradox Valley, Colorado induced seismicity dataset as an ideal test case: a single, high-pressure injector that has induced >7000 earthquakes between 1991 and 2012. We find that injection-driven earthquakes are approximately $22\pm 5\%$ of the total catalog and have distinct spatiotemporal clustering with a larger b-value, closer proximity to the well and earlier occurrence in the injection history. Our model may be applicable to other regions to help determine site's susceptibility to triggered earthquakes due to fluid injection.

Plain Language Summary

The Paradox Valley Unit, Colorado in the central United States has had a remarkable increase in seismicity coincident with over 8 million cubic meters of brine fluid injection since 1991, inducing >7000 earthquakes within an aquifer 4.5 km below the surface. We use a physics-based model of the Earth combined with statistical and machine learning techniques to help discern which earthquakes are triggered by other earthquakes and which earthquakes are directly triggered by the stress changes from the well as well as their comparative characteristics. Discerning which earthquakes are directly caused from pressure changes due to the fluid injected by the well can inform our understanding of earthquake physics and provide useful information to operators of energy production sites.

1 Introduction

A variety of anthropogenic industrial activities, including wastewater disposal, can induce seismicity (Ellsworth, 2013; Keranen et al., 2014; Shirzaei et al., 2016). Similar to naturally occurring earthquakes, induced seismicity typically occurs on pre-existing, critically stressed faults (Townend & Zoback, 2000). Generating induced seismicity from the reactivation of faults is attributed to several physical mechanisms: pore pressure diffusion (Keranen & Weingarten, 2018; Weingarten et al., 2015; Langenbruch et al., 2018),

46 poroelastic coupling (Segall & Lu, 2015), and stress changes caused by seismic or aseis-
47 mic fault slip (Ge & Saar, 2022; Brown & Ge, 2018).

48 These physical mechanisms for induced seismicity jointly contribute to the trigger-
49 ing potential of each earthquake. Since induced earthquakes can be triggered by small
50 stress changes of order 1-10 kPa (Bachmann et al., 2012; Cacace et al., 2021; Stokes et
51 al., 2023), a large difficulty arises in deciphering which mechanism was responsible for
52 triggering each earthquake. We are particularly interested in discerning which earthquakes
53 were more likely driven by injection-related stress changes and which earthquakes were
54 more likely driven by stress changes from prior earthquakes. Furthermore, site-to-site
55 differences in physical rock properties, reservoir structure, fault geometry, and remnant
56 tectonic stress could contribute to differences in the ratio of injection-driven and earthquake-
57 driven events despite similar injection-related stresses.

58 Relative stress changes from fluid injection require analytical or numerical mod-
59 els to resolve the spatio-temporal evolution of pore pressure and poroelastic stress. To
60 capture the fully coupled poroelastic stress changes (Biot, 1941; Rice & Cleary, 1976;
61 Wang, 2000) induced from the fluid sources requires detailed knowledge of the hydro-
62 geologic properties of the region. The fault geometry is also critical for resolving fault
63 plane stress tractions that characterize fault stability and the potential for induced seis-
64 micity (G. C. P. King et al., 1994; Cocco, 2002; Levandowski et al., 2018). Hence, any
65 attempt at discerning induced earthquakes requires an accurate and comprehensive hy-
66 drogeological model, detailed injection well data, precise fault geometries, and high-resolution
67 earthquake catalog.

68 Here, we investigate which earthquakes are more likely triggered by stress changes
69 from injection and which earthquakes are more likely triggered by earthquake-earthquake
70 interaction. We built a three-dimensional (3D) fully-coupled poroelastic model of Para-
71 dox Valley Unit, CO (PVU) to resolve time-dependent pore pressure and stress changes
72 due to brine injection. To inform the contribution of our earthquake triggering mech-
73 anisms, we use a random forest regression machine learning analysis trained on more than
74 20 years of induced earthquakes at Paradox Valley Unit and SHapley Additive exPla-
75 nations (SHAP), a game theoretic approach to explain the output of any machine learn-
76 ing model (Lundberg & Lee, 2017). We corroborate our results with an independent, in-
77 duced seismicity cluster analysis, which demonstrates that the physics-based machine

78 learning method provides novel insight into discerning triggering mechanism not previ-
79 ously captured. This model explores the induced earthquake triggering process for wastew-
80 ater disposal and could help discern what regions are more or less susceptible to stress
81 changes from anthropogenic sources with applicability to other types of subsurface in-
82 jection including CO₂ sequestration, enhanced geothermal systems, and hydraulic frac-
83 turing.

84 **2 Paradox Valley Unit (PVU) Data**

85 The PVU is a program run by the U.S. Bureau of Reclamation, which has been dis-
86 posing deep brine into a confined aquifer between 4.3 and 4.6 km depth in Paradox Val-
87 ley, Colorado since 1995 (Ake et al., 2005; Denlinger & RH O’Connell, 2020) (Figure 1).
88 The high-pressure fluid injection has been associated with >7000 earthquakes between
89 1991 and 2012, which have all been documented as induced seismicity (Ake et al., 2005;
90 Block et al., 2015; V. M. King et al., 2016; Denlinger & RH O’Connell, 2020). Most seis-
91 mic events within 5 km of the injection well were induced within the first 10 years of in-
92 jection and nearly all within the high permeability injection reservoir known as the Leadville
93 formation. This zone is highly pressurized from decades of continuous pumping and dic-
94 tates the lateral migration of seismicity away from the wellbore. These carefully stud-
95 ied events support the notion of a \sqrt{t} diffusion model for pressurization from the well
96 (Block et al., 2015; V. M. King et al., 2016) (Figure 2). Additional ancillary data also
97 make this an ideal study region: numerous wells that extend into deeper formations than
98 just the Leadville aquifer, 3D seismic tomography, logs of P-wave velocity, density and
99 porosity from the near surface to basement in the injection well, and logging of geologic
100 units in other wells in the area (Denlinger & RH O’Connell, 2020).

101 Most importantly for our purposes, previous work has already compiled a detailed,
102 fully coupled poroelastic model (Denlinger & RH O’Connell, 2020). This model is given
103 by a grid description of nodes with corresponding parameter values which we validate
104 in our finite element numerical model (Dassault Systemes, 2020) with improved mesh-
105 ing near the well where pressure and stress gradients are highest (see SM 8.1). Figure
106 2 includes a plot of the earthquake distribution overlaid on a cross-section of the numer-
107 ical model mesh.

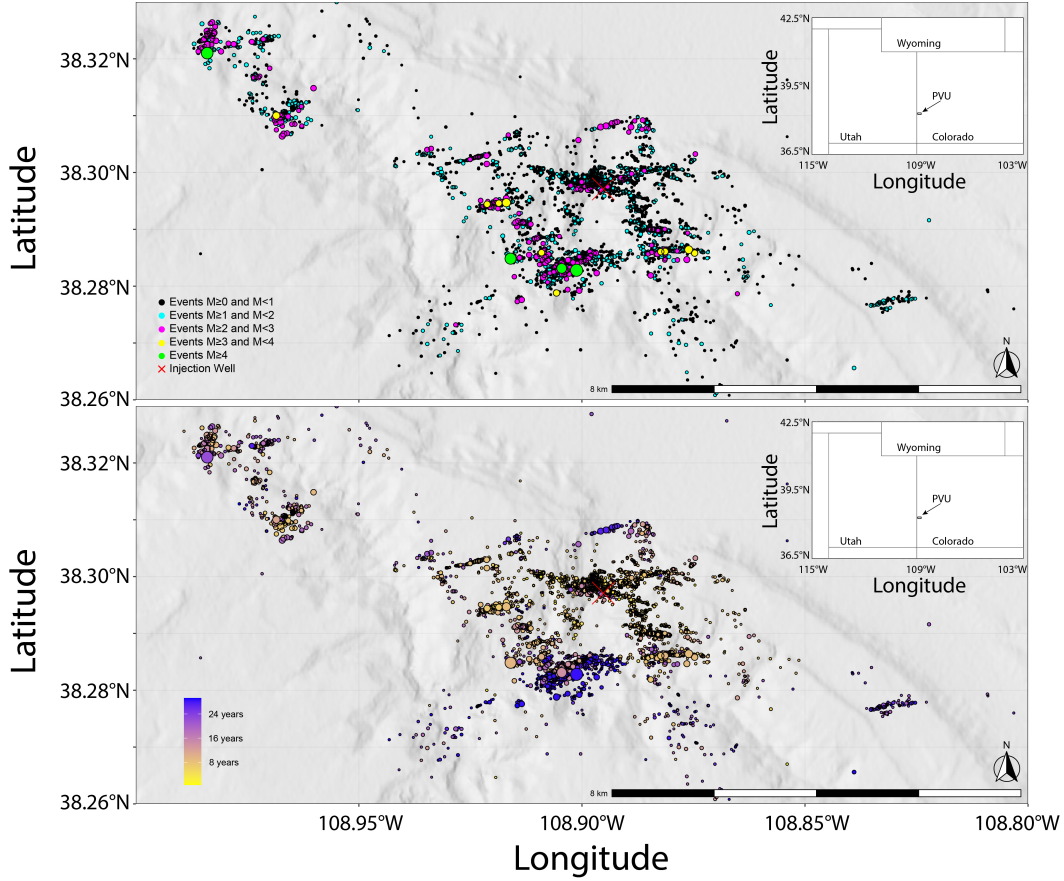


Figure 1. Regional setting of the Paradox Valley Unit, CO (PVU). a) Earthquakes binned by different magnitude ranges. The well is denoted by the red ‘X’. The deep brine injection began in 1991 at a depth of 4.3 km. Most seismicity is clustered near the well, where stress perturbations are largest and fluctuate the most. b) Temporal evolution of events. There are more than 7000 earthquakes in the catalog, but within the 8 km radius around the well which we use for analysis includes only 3000.

108 **3 Methods**

109 The core of our methodology relies on the careful development of machine learn-
 110 ing features which will represent the contribution of injection-driven stress changes and
 111 earthquake-driven stress change for each event in the PVU catalog. Our injection-driven
 112 stress feature is resolved using time-dependent pore pressure and stress changes through-
 113 out the PVU. Pore pressure and stress perturbations are used to produce von Mises stress
 114 features that are physical inputs for the ML/SHAP analysis. To quantify our earthquake-
 115 driven stress changes, we create a second feature in the ML/SHAP analysis, which we

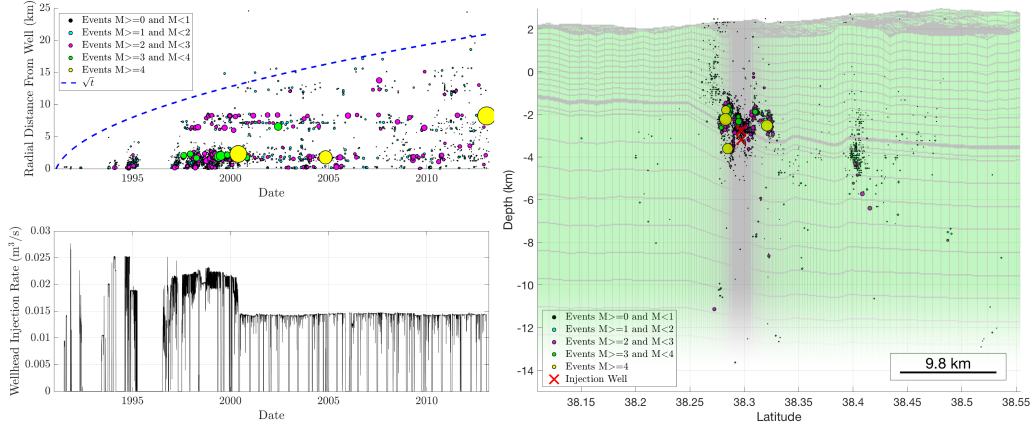


Figure 2. Earthquakes plotted as their radial distance from the well and time. Most earthquakes behave in a typical \sqrt{t} diffusion rate away from the well consistent with progressive lateral migration of seismicity through the permeable Leadville (Ake et al., 2005; Block et al., 2015; Denlinger & RH O’Connell, 2020). Flow tests were performed prior to 1995. Notice injection is highest during peak injection rates ~ 1997 . Our model records pore pressure and stress perturbations from 10-July-1991 to 16-April-2013. Numerical model cross section with earthquake and well depth superimposed. The model is a fully-coupled poroelastic model based on prior work (Denlinger & RH O’Connell, 2020). We increase the grid discretization near the well to capture large changes in pressure gradients (see SM 8.1).

116 call the "earthquake feature". The earthquake feature is calculated from the stresses pro-
 117 duced by prior earthquakes that may have generated perturbations large enough to pro-
 118 duce the current earthquake. These two feature weights are then trained on the entire
 119 PVU catalog to find the optimal weight of each feature for each earthquake in the PVU
 120 catalog. SHAP analysis of the ML model’s feature weights allow for interpretation of the
 121 relative contribution of each feature to each event. We support our interpretations of trig-
 122 gering mechanisms from the ML/SHAP with results from a nearest neighbor distance
 123 cluster analysis.

124 3.1 Numerical Model

125 We model the relative increase in pore pressure ΔP (scalar) and poroelastic stress
 126 ΔS (2nd order tensor) for the PVU using a model with one injection well in the center
 127 of the model domain (SM Figure 1). The hydrogeologic structure is based on a nodal

128 distribution of parameters that we reduced down to 1000 unique unit formations and use
 129 Abaqus to resolve the linear poroelastic equations (R. G. Hill et al., 2024) (see SM 8.1).
 130 The model dimensions are 50 km by 50 km laterally with a 18 km depth. Figure 2 shows
 131 a cross-section through the well injection zone. The injection is divided across three per-
 132 forated zones consistent with prior modeling and uses the entire injection history as 7952
 133 unique daily rates in our model from 10-July-1991 to 16-April-2013 (Denlinger & RH O’Connell,
 134 2020) (Figure 2). We output ΔP and ΔS from these daily steps across the entire do-
 135 main at 284 \sim monthly time steps. We do not include earthquakes in our study that oc-
 136 cur outside of the modelled time domain which is restricted by the injection history, al-
 137 though the earthquake catalog does extend until 31-December-2019 (Figure 2).

138 **3.2 Stress Features**

139 The Abaqus outputs of ΔP and ΔS were post-processed in Matlab using `abaqus2matlab`
 140 (Papazafeiropoulos et al., 2017). The stress features of ΔP and ΔS represent the rel-
 141 ative change induced from the fluid injection and are resolved at the closest value in the
 142 domain to each \sim 3000 earthquakes during our study time. We assessed a variety of dif-
 143 ferent stress features during the preliminary stages of this work, consistent with prior
 144 forecasting studies (DeVries et al., 2018; Sharma et al., 2020; Qin et al., 2022). We found
 145 that von Mises stress and von Mises stressing rate were the best stress-based features
 146 for forecasting the seismicity rate and are the only two stress features we consider here-
 147 inafter. We make the assumption that the von Mises stress is resolved uniformly using
 148 a strike azimuth of 260° and vertical dip consistent with the most common faulting struc-
 149 ture present from the earthquakes locations (Denlinger & RH O’Connell, 2020).

150 **3.3 Earthquake Feature**

151 Static stress transfer modeling can be used to assess earthquake-earthquake trig-
 152 gering on faults embedded in an elastic half space with homogeneous isotropic elastic prop-
 153 erties (Lin & Stein, 2004; Toda et al., 2005). Stress transfer can promote or reduce the
 154 potential of earthquake triggering, depending on the coefficient of friction, fault geom-
 155 etry, and sense of slip (G. C. P. King et al., 1994; Stein, 1999). Since the exact geome-
 156 tries of every earthquake in our model are unknown, we choose to develop an earthquake
 157 feature that is based on the occurrence of prior earthquakes that could have plausibly
 158 influenced each earthquake.

159 We use ‘cutde’ (Thompson, 2021) to resolve elastic stress transfer produced from
 160 triangular dislocation element representations of fault slip (Nikkhoo & Walter, 2015).
 161 Several assumptions are required for the static stress transfer modeling: (1) We assume
 162 a uniform stress drop for every event of 3 MPa, (2) a shear modulus of 30 GPa, and (3)
 163 a Poisson ratio of 0.25. Under this framework we show that the von Mises stress is self-
 164 similar for both parallel and perpendicular receiver receiver planes at a given distance
 165 from the event (SM Figure 2). By varying event magnitude, we calculate a radius from
 166 the center of the dislocation that can increase the potential of failure up to a distance
 167 that intersects the 10 kPa triggering threshold (Reasenberg & Simpson, 1992; Stein, 1999).
 168 As a sensitivity test we varied the stress drop from 1-10 MPa and observe marginal change
 169 to the perturbable radius for varying magnitudes (SM Figure 2). Then, for every earth-
 170 quake, we create an earthquake-to-earthquake feature, which counts the number of earth-
 171 quakes that could have perturbed it. The earthquake count is represented by $\ln(N +$
 172 $1)$, where N is the number of perturbing earthquakes to have occurred prior to each event.
 173 Higher values of this feature indicate a higher likelihood of earthquake-earthquake in-
 174 teraction.

175 3.4 ML/SHAP Analysis

176 We use the machine learning technique of random forest regression (RFR) to fit
 177 our observed seismicity (Ho et al., 1995; Ho, 1998). The RFR model makes a prediction
 178 on the target variable, which are one-hot encoded occurrences of the observed earthquakes
 179 across 284 \sim monthly time steps each. We avoid overfitting and optimize model hyper-
 180 parameters using an exhaustive grid search applied to a 5-fold cross-validation score. The
 181 observed seismicity is therefore repeatedly divided into training and test folds with the
 182 mean squared error evaluating fit on the test folds which the trained model does not see.
 183 The RFR models chosen for our analysis were trained using the hyperparameters derived
 184 from the best-performing model during the cross-validation process.

185 The input features are composed from the stress and earthquake features as well
 186 as their time lags. The time lags are introduced both to capture any potential anisotropy
 187 or hydromechanical heterogeneity that are not explicit in the numerical model as well
 188 as time delayed effects that former earthquakes or stress history may have when perturb-
 189 ing the current earthquake. We find that including more lags improves the overall fit of
 190 our model, up to \sim 50 lags, but is likely over-fitting and unrealistic. We assume that the

191 physical meaning of the lags are unreasonable beyond ~ 1 year before the actual earth-
 192 quake timing and reserve our total lags to the local minimum of 5 lags (SM Figure 3).
 193 In other words, a model can contain the current stress/earthquake feature (+0 lag), the
 194 time period prior (+1 lag), and the time periods before that (+2-+5 lag etc..) or any
 195 combination of that set (SM Figure 3).

196 To assess feature importance, we use SHAP, which provides a robust and self-consistent
 197 means to explain the predictions of our target variable (earthquake or no-earthquake)
 198 by computing the contribution of each feature to the prediction (Shapley et al., 1953;
 199 Lundberg & Lee, 2017). A key advantage of SHAP lies in its ability to consistently un-
 200 tangle the impacts of multiple correlated input variables (Trugman & Ben-Zion, 2023).
 201 Since the SHAP value is represented as an additive feature, it is a linear model and the
 202 contributions of each feature can be added to describe the contribution that the stress
 203 features have compared to the earthquake features. This is often preferable compared
 204 to permutation feature importance which chooses importance based on the decrease in
 205 model performance. Larger SHAP values for a given feature, averaged across the dataset,
 206 signify a higher importance for the model's prediction.

207 3.5 Cluster Analysis

208 As an independent test of earthquake behavior, we investigate how the PVU seis-
 209 micity is distributed in magnitude, space, and time using a traditional cluster analysis.
 210 We use the nearest neighbor distance (NND) in the space-time-magnitude domain (Baiesi
 211 & Paczuski, 2004) for each pair of events i and j using the following equation:

$$\eta_{ij} = \begin{cases} t_{ij}(r_{ij})^d 10^{-bm_i}, & t_{ij} > 0; \\ \infty, & t_{ij} \leq 0 \end{cases} \quad (1)$$

212 Where, t_{ij} is the interevent time (year), r_{ij} is the inter event distance (km), d is the di-
 213 mension of the earthquake hypocenter distribution ($d = 1.32$) determined using a box-
 214 counting procedure (Corral, 2003) (SM Figure 4), b is the b-value ($b = 0.75$) determined
 215 by maximum likelihood estimation (Aki, 1965), and m_i is the i th event magnitude (Zaliapin
 216 & Ben-Zion, 2013; Schoenball et al., 2015). The NND is separable into rescaled distance
 217 (R_{ij}) and rescaled time (T_{ij}) where (Zaliapin et al., 2008; Zaliapin & Ben-Zion, 2013):

$$\eta_{ij} = R_{ij}T_{ij} \quad (2)$$

$$R_{ij} = (r_{ij})^d 10^{-bm_i/2} \quad (3)$$

218

$$T_{ij} = (r_{ij})^d 10^{-bm_i/2}, \quad (4)$$

220 An advantage of this form of NND is that the clustering style of seismicity can be dis-
 221 played by a joint 2D distribution of rescaled time $\log_{10} T_{ij}$ and rescaled distance $\log_{10} R_{ij}$
 222 (Zaliapin et al., 2008; Zaliapin & Ben-Zion, 2013, 2016). The distribution helps to de-
 223 scribe the type of earthquake clustering style, since observed seismicity often shows a bi-
 224 modal joint distribution divided by a constant line and chosen nearest-neighbor thresh-
 225 old n_0 . Events below this threshold are classified as clustered (i.e., earthquake-driven trig-
 226 gering) and the events that are above this threshold are classified as background (i.e.,
 227 injection-driven or independent) (Zaliapin & Ben-Zion, 2016). We use the NND distri-
 228 butions for the PVU as an independent test of the physical mechanism driving each earth-
 229 quake in the sequence. We hypothesize that our ML/SHAP model will preferentially sep-
 230 arate injection-driven vs earthquake-driven events as identified by Zaliapin and Ben-Zion
 231 (2016).

232 4 Results

233 4.1 Numerical Model Results

234 The fully-coupled poroelastic model shows that areas with seismicity experience
 235 pore pressure increases from 0.005 MPa to 9 MPa. Most pore pressure increases occur
 236 within an 8 km radius around the injection well (SM Figures 5-10). Most seismicity oc-
 237 curs in close vicinity of the injection well and the ΔP is highest in early 1999 (~ 9 MPa).
 238 The pressure changes near the well mimic injection rate changes as the temporal delay
 239 of diffusion is negligible. Elsewhere, the diffusion process dominates the pressure changes
 240 and therefore the increase in pore pressure is more gradual through time (SM Figure 8-
 241 9). Across the domain, seismicity occurs during the highest rates of pressure increase.
 242 This observation is consistent with other instances of wastewater induced seismicity (Langenbruch
 243 et al., 2018; Qin et al., 2022). The increasing pore pressure diffuses laterally through the
 244 highly permeable Leadville formation. Low permeability confining units above and be-
 245 low the reservoir restrict vertical pressure migration (SM Video 1).

246 **4.2 Cluster Analysis Results**

247 Results of the NND cluster analysis show that a larger portion of the earthquakes
 248 are classified as the background mode (Zaliapin & Ben-Zion, 2016; Goebel et al., 2019)(Fig-
 249 ure 3a). The constant threshold value $\eta_0 = -4.9$ is chosen based on a 1D Gaussian mix-
 250 ture model analysis (Zaliapin et al., 2008; Zaliapin & Ben-Zion, 2016). The clustering
 251 behavior is similar to other cases of wastewater induced seismicity (Zaliapin & Ben-Zion,
 252 2016; Glasgow et al., 2021). There is a larger population of background events and clus-
 253 tered events occur at short space-time distances. These results are also dissimilar from
 254 other cases of induced seismicity that have a more clear bimodal distribution, albeit dif-
 255 ferent mechanical processes are occurring (Zaliapin & Ben-Zion, 2016, e.g., Coso and Salton
 256 Sea geothermal areas). A small portion of the background domain is characterized by
 257 low R_{ij} and large T_{ij} , which often characterizes these events as repeaters (Zaliapin &
 258 Ben-Zion, 2016; Hsu et al., 2024). These events make sense in the context of single well
 259 injection. The start-stop nature of the injection means repetitive changes in stress oc-
 260 cur at the same locations. This is observed in the pore pressure results at different clus-
 261 ters near the well where the pore pressure closely follows the flux of the injection (SM
 262 Figures 5-8).

263 **4.3 ML/SHAP Model Results**

264 Our preferred model uses the following: 1000 total trees, a maximum depth of 10,
 265 a minimum sample split of 10, and a minimum of 4 samples for a leaf node. Figure 4a
 266 shows the fit of our random forest model for two different model types. One model uses
 267 only the von Mises stress rate and earthquake feature while the other model uses both
 268 the von Mises stress and the von Mises stress rate as well as the earthquake feature (in-
 269 cluding lags). We find that the mean squared error (MSE) is slightly lower for the model
 270 that includes both stress features. However, we choose to present the parsimonious so-
 271 lution of one stress feature and refer the reader to the supplementary for the results in-
 272 cluding both stress features, which contains small differences to the main results (SM
 273 Figures 11-14).

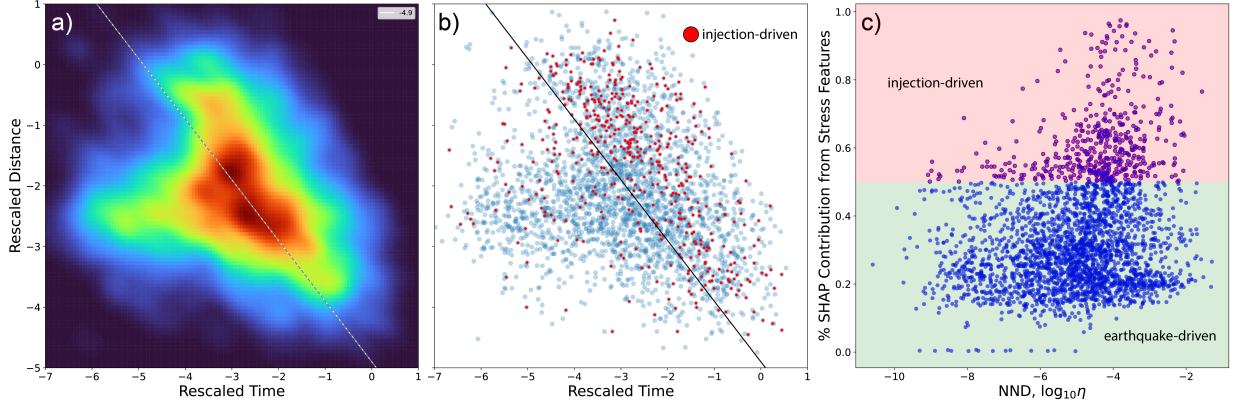


Figure 3. a) Nearest neighbor time-distance distributions for seismicity in the PVU. The color bar represents the number of event pairs. The total number of earthquakes used in this analysis is 2927. The diagonal dashed line is the η_0 background (above) and clustered (below) mode threshold. The value is a constant distance threshold determined by the 1D Gaussian mixture model and is -4.9. b) Comparing the earthquakes that have at least 50% stress feature contribution on the rescaled distance rescaled time plot. Many of the earthquakes cluster in the independent background mode with a second distribution towards the repeater mode and a few earthquakes spread out in the cluster mode. c) The SHAP stress feature contribution vs. the nearest neighbor distance value. Many of the earthquakes cluster below the 50% stress feature contribution indicating and to the left of the -4.9 cluster threshold. However, earthquakes that have >50% stress feature contribution, denoted as red circles, tends to populate the ‘background’ mode of the NND (to the right of -4.9). These results are consistent for earthquakes driven by stress from the injection since they act as initial parent earthquakes that trigger subsequent seismicity in a region that has experienced stress changes high enough to begin seismicity.

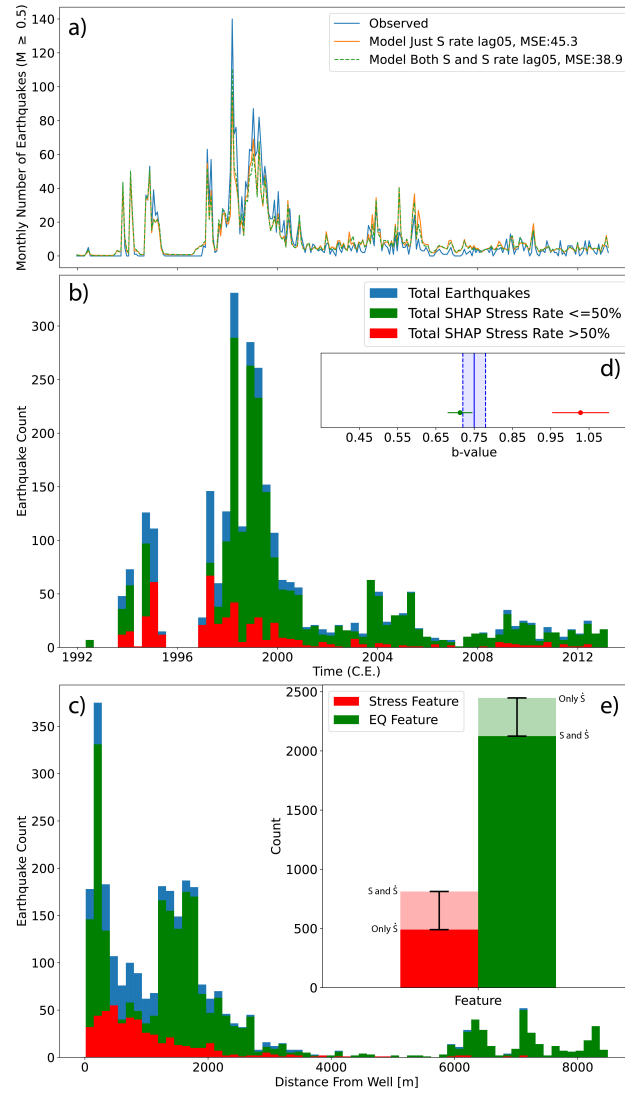


Figure 4. a) Forecasted seismicity rate across for all time steps. Orange line represents the best fit model that includes only the von-Mises stress rate. The dashed green line includes von-Mises stress and has slightly better fit. b) Earthquake count binned through time for earthquakes with SHAP stress rate $\leq 50\%$ (ie. earthquake-driven green) and $> 50\%$ (ie. injection-driven red). c) same as panel b, but for distance away from well. d) b-value analysis of all earthquakes (blue), earthquake-driven (green), and injection-driven (red). e) Ratio of all earthquakes with a larger sum of SHAP value for stress features (red) and the earthquake features (green). We reflect the uncertainty of triggering mechanism based on our two models described in panel a.

274 The SHAP analysis results are summarized in SM Figure 15. We output the re-
 275 sults exclusively at the time when the earthquakes occur since we are only interested in
 276 discerning the contribution of the stress features at that time. A summary of the SHAP
 277 contributions for all time, not just when the earthquakes occur, is presented in the sup-
 278 plementary material (SM Figure 16). The feature with the higher overall impact on the
 279 model is the perturbable earthquake feature that represents the number of earthquakes
 280 that occurred during the chosen time step that could have potentially perturbed the earth-
 281 quake in question. The next most important features, with nearly equal importance, are
 282 the lagged von Mises stress rates. These stress features are considerably less important
 283 on average compared with the earthquake feature.

284 To assess the total contribution of the stress features vs the earthquake features,
 285 we compare the cumulative feature results. Separating which earthquakes are dominated
 286 by cumulative feature importance, Figure 4e shows that the ratio of earthquakes that
 287 have a higher stress feature contribution compared to earthquakes that have a higher to-
 288 tal earthquake feature contribution is about 1:5. We examined the sensitivity of this since
 289 it would be expected that increasing lags may contribute to higher contribution to stress.
 290 While the stress contribution does increase for models that include 0,+1,+2 lags, after
 291 the model reaches +3 lags, earthquakes that are considered to have a higher total stress
 292 contribution increase marginally. For example, from +3 lags to +5 lags the ratio has a
 293 percent increase of only $\sim 0.5\%$ (SM Figure 17). We do not pursue sensitivity past +5
 294 lags as the SHAP analysis is computationally expensive with increasing features. It is
 295 important to note that when testing increasing lag sensitivity, the overall ratio of the to-
 296 tal number of stress features to earthquake features remains the same.

297 **5 Discussion**

298 The ML/SHAP model identifies injection-driven earthquakes (ie. $>50\%$ stress fea-
 299 ture contribution) predominantly as background events in the NND model (Figure 3b-
 300 c). In the NND model, background events are mostly the independent Poisson mode (Zaliapin
 301 et al., 2008; Zaliapin & Ben-Zion, 2016). This suggests injection-driven earthquakes of-
 302 ten act as parent earthquakes, likely induced by pore pressure and stress changes, trig-
 303 gering further seismicity. These results are further supported by the relative timing of
 304 these earthquakes, which often occur at the beginning of injection stages (Figure 4b).
 305 We statistically compare injection-driven event distribution to the larger catalog using

306 a two-sample Kolmogorov–Smirnov test, which rejects the null hypothesis of identical
307 distributions with 99% confidence (SM Figure 18).

308 We explored two interevent time measures to analyze event timing between injection-
309 driven and earthquake-driven classes (Davidsen et al., 2021). The first measure, interevent
310 time ratio R , indicates deviations from a Poisson process (Van Der Elst & Brodsky, 2010;
311 Davidsen et al., 2017). Rejecting the Poisson process hypothesis with >95% confidence,
312 we observe a significant peak at $R = 0$ suggesting triggering, and another at $R = 1$
313 indicating longer intervals likely due to stress changes stimulated by a non-random pro-
314 cess (SM Figure 19). Injection-driven earthquakes show less bi-modal distribution, im-
315 plying less temporal clustering than earthquake-driven ones. The second measure, the
316 Bi-test, also indicates temporal clustering and rejects the Poisson process hypothesis with
317 >95% confidence (Bi et al., 1989; Baró et al., 2014). Injection-driven earthquakes ex-
318 hibit lower temporal clustering (lower fluctuation in H values) compared to clearly clus-
319 tered earthquake-driven ones (higher fluctuation in H values around 0 and 1) (SM Fig-
320 ure 20).

321 We also analyze the spatiotemporal distribution of injection-driven earthquakes (Fig-
322 ure 4b-c). They tend to occur earlier in injection history and cluster near the injection
323 well, contrasting with earthquake-driven earthquakes. These events coincide with sharp
324 stress field changes near the well, often preceding clustered seismicity. The b-value of injection-
325 driven earthquakes (Figure 4d) is notably higher (1.03) compared to overall seismicity
326 (0.75) and earthquake-driven events (0.71). This suggests that injection-driven events
327 tend to have lower magnitudes, on average, than the earthquake-driven events and a b-
328 value closer to 1 indicates that these events may appear to mimic independent background
329 events. The finding that earthquake-driven events produce lower b-values and charac-
330 terize more of the large events in induced catalogs may have implications for maximum
331 magnitude estimates of induced earthquakes, since initial injection-driven earthquakes
332 at the onset of induced sequences might underestimate the overall maximum magnitude
333 of triggered seismicity

334 Clusters of seismic activity away from the well are noticeable, yet they have fewer
335 stress-dominated earthquakes (SM Figure 21). Often, clusters away from the well are ini-
336 tiated by a few injection-driven earthquakes. This observation is consistent with the ma-
337 chine learning process since earthquakes that had no prior earthquakes would not be ex-

338 pected to have a strong prior earthquake feature contribution. However, not all injection-
339 driven earthquakes precede nearby seismic events. Additionally, areas lacking clear clus-
340 tering seem to host multiple injection-driven earthquakes, suggesting varied driving mech-
341 anisms in those regions (SM Figure 21).

342 It is important to recognize that uncertainty is introduced in the model at various
343 stages: physical model material parameters, static stress transfer parameters, RFR in-
344 put features, and the number of included lags. We affirm the numerical model (see SM
345 8.1 and SM Figures 5-10) and show that the static stress transfer at a triggering thresh-
346 old of 10 kPa is only marginally sensitive to varied stress drop assumptions (SM Figure
347 2). We find that increasing lags beyond +3 does not greatly change the ratio of injection-
348 driven and earthquake-driven earthquakes (SM Figure 17). The main model sensitivity
349 lies in input features: incorporating von Mises stress and rate increases injection-driven
350 earthquakes from 17% to 27% (Figure 4e and SM Figure 14). It is unclear whether in-
351 cluding both the stress and stress rate features provides a better model since more injection-
352 driven earthquakes also begin to populate the cluster mode, which we assume is a prod-
353 uct of over-fitting the seismicity rate (Figure 4a and SM Figure 13). We therefore sug-
354 gest that these two models may provide estimates on the lower and upper bound with
355 the true portion of injection-driven earthquakes at approximately $22\pm 5\%$ of the total.

356 Results of this study indicate that the physics-based model, with RFR and SHAP
357 analysis, accounts for a significant portion of independent background mode events found
358 in NND cluster analysis. However, not all background mode events are classified as injection-
359 driven. The absence of a clear bi-modal distribution in NND analysis suggests that events
360 populating the independent background mode may have less direct fluid injection influ-
361 ence (Zaliapin & Ben-Zion, 2016; Glasgow et al., 2021). We expect this ratio of injection-
362 driven vs earthquake-driven seismicity to vary by geologic region, stress state, distribu-
363 tion of preexisting faults, and injection style. Understanding this ratio is crucial for wastew-
364 ater management, as it impacts induced seismic hazard. Sites where seismicity is mainly
365 earthquake-driven would be harder to control via well operations best practices (R. G. Hill
366 et al., 2024), while sites with mostly injection-driven events may be more manageable.
367 Identifying the triggering process in candidate sites can guide energy production deci-
368 sions, avoiding areas prone to severe triggered seismicity.

369 **6 Conclusion**

370 We decipher induced earthquake triggering mechanisms using a 3D fully-coupled
371 poroelastic model of brine injection and a random forest machine learning model trained
372 on more than 20 years of induced earthquakes at Paradox Valley Unit, Colorado. Our
373 simple ML/SHAP feature training approach, using one injection-driven feature and one
374 earthquake-driven feature, allows for the separation of events that are more likely injection-
375 driven from events that are more likely earthquake-driven in the sequence. Comparing
376 the ML/SHAP results with a nearest-neighbor cluster analysis reveals good agreement
377 in stress contribution and cluster style. Our methodology finds that injection-driven earth-
378 quakes make up only $22\pm 5\%$ of the catalog and have distinct spatiotemporal clustering
379 with a larger b-value, closer proximity to the well and earlier occurrence in the injection
380 history. Our method may be applicable to other regions to help determine the site sus-
381 ceptibility to earthquake triggering or aid in declustering induced catalogs.

382 **7 Open Research**

383 Data of Abaqus files, post-processing scripts, ML model scripts, and figure gener-
384 ation scripts are available online at Hill, R. (2024) ([https://doi.org/10.5281/zenodo](https://doi.org/10.5281/zenodo.10967359)
385 [.10967359](https://doi.org/10.5281/zenodo.10967359)).

386 The wastewater injection data and earthquake data is available from the Bureau
387 of Reclamation Upper Colorado Basin website ([https://www.usbr.gov/uc/](https://www.usbr.gov/uc/progact/paradox/index.html)
388 [progact/paradox/index.html](https://www.usbr.gov/uc/progact/paradox/index.html)).

389 The numerical models were built and solved using the software Abaqus (Dassault Sys-
390 temes, 2020).

391 **Acknowledgments**

392 The authors appreciate discussion with Robert Guyer at early stages of the work. We
393 acknowledge use of the CSRC high-performance computing cluster and other support
394 from San Diego State University. D.T.T acknowledges support from NSF Award EAR-
395 2121666.

396 **References**

397 Ake, J., Mahrer, K., O'Connell, D., & Block, L. (2005). Deep-injection and closely

- 398 monitored induced seismicity at paradox valley, colorado. *Bulletin of the Seis-*
 399 *mological Society of America*, 95(2), 664–683.
- 400 Aki, K. (1965). Maximum likelihood estimate of b in the formula $\log n = a - bm$ and
 401 its confidence limits. *Bull. Earthquake Res. Inst., Tokyo Univ.*, 43, 237–239.
- 402 Bachmann, C. E., Wiemer, S., Goertz-Allmann, B., & Woessner, J. (2012). Influ-
 403 ence of pore-pressure on the event-size distribution of induced earthquakes.
 404 *Geophysical Research Letters*, 39(9).
- 405 Baiesi, M., & Paczuski, M. (2004). Scale-free networks of earthquakes and after-
 406 shocks. *Physical review E*, 69(6), 066106.
- 407 Baró, J., Martín-Olalla, J.-M., Romero, F. J., Gallardo, M. C., Salje, E. K., Vives,
 408 E., & Planes, A. (2014). Avalanche correlations in the martensitic transition of
 409 a cu-zn-al shape memory alloy: Analysis of acoustic emission and calorimetry.
 410 *Journal of Physics: Condensed Matter*, 26(12), 125401.
- 411 Bear, J. (1988). *Dynamics of fluids in porous media*. Courier Corporation.
- 412 Bi, H., Börner, G., & Chu, Y. (1989). Correlations in the absorption lines of the
 413 quasar q0420-388. *Astronomy and Astrophysics (ISSN 0004-6361)*, vol. 218,
 414 no. 1-2, July 1989, p. 19-23., 218, 19–23.
- 415 Biot, M. A. (1941). General theory of three-dimensional consolidation. *J.*
 416 *Appl. Phys.*, 12(2), 155–164. Retrieved 2021-04-13, from [https://
 417 urldefense.com/v3/_http://aip.scitation.org/doi/10.1063/
 418 1.1712886_;;!Mih3wA!E0xCUAX3ctL8wKS_tp-pNn95UaeXh_lRky7b2Mcg4
 419 -S1_-Ss2N0b2nM51d42UzHIa8rqXMPiIajp0q38i\\$](https://urldefense.com/v3/_http://aip.scitation.org/doi/10.1063/1.1712886_;;!Mih3wA!E0xCUAX3ctL8wKS_tp-pNn95UaeXh_lRky7b2Mcg4-S1_-Ss2N0b2nM51d42UzHIa8rqXMPiIajp0q38i$) doi: 10.1063/1.1712886
- 420 Block, L. V., Wood, C. K., Yeck, W. L., & King, V. M. (2015). Induced seismicity
 421 constraints on subsurface geological structure, paradox valley, colorado. *Geo-*
 422 *physical Journal International*, 200(2), 1172–1195.
- 423 Brown, M. R., & Ge, S. (2018). Small earthquakes matter in injection-induced seis-
 424 micity. *Geophysical Research Letters*, 45(11), 5445–5453.
- 425 Cacace, M., Hofmann, H., & Shapiro, S. A. (2021). Projecting seismicity induced
 426 by complex alterations of underground stresses with applications to geothermal
 427 systems. *Scientific Reports*, 11(1), 23560.
- 428 Cocco, M. (2002). Pore pressure and poroelasticity effects in coulomb stress analysis
 429 of earthquake interactions. *J. Geophys. Res.*, 107, 2030.
- 430 Corral, A. (2003). Local distributions and rate fluctuations in a unified scaling law

- 431 for earthquakes. *Physical Review E*, *68*(3), 035102.
- 432 Dassault Systemes, . (2020). *Abaqus (version 2019)*. Retrieved from [https://](https://urldefense.com/v3/_https://www.3ds.com/products-services/simulia/products/abacus/_;!!Mih3wA!EOxCUax3ctL8wKS.tp-pNn95UaeXh_lRky7b2Mcg4-S1_-Ss2N0b2nM5ld42UzHIa8rqXmpIag2Io7P8$)
- 433 [urldefense.com/v3/_https://www.3ds.com/products-services/](https://urldefense.com/v3/_https://www.3ds.com/products-services/simulia/products/abacus/_;!!Mih3wA!EOxCUax3ctL8wKS.tp-pNn95UaeXh_lRky7b2Mcg4-S1_-Ss2N0b2nM5ld42UzHIa8rqXmpIag2Io7P8$)
- 434 [simulia/products/abacus/_;!!Mih3wA!EOxCUax3ctL8wKS.tp-pNn95UaeXh](https://urldefense.com/v3/_https://www.3ds.com/products-services/simulia/products/abacus/_;!!Mih3wA!EOxCUax3ctL8wKS.tp-pNn95UaeXh_lRky7b2Mcg4-S1_-Ss2N0b2nM5ld42UzHIa8rqXmpIag2Io7P8$)
- 435 [_lRky7b2Mcg4-S1_-Ss2N0b2nM5ld42UzHIa8rqXmpIag2Io7P8\\$](https://urldefense.com/v3/_https://www.3ds.com/products-services/simulia/products/abacus/_;!!Mih3wA!EOxCUax3ctL8wKS.tp-pNn95UaeXh_lRky7b2Mcg4-S1_-Ss2N0b2nM5ld42UzHIa8rqXmpIag2Io7P8$)
- 436 Davidsen, J., Goebel, T., Kwiatek, G., Stanchits, S., Baró, J., & Dresen, G. (2021).
- 437 What controls the presence and characteristics of aftershocks in rock frac-
- 438 ture in the lab? *Journal of Geophysical Research: Solid Earth*, *126*(10),
- 439 e2021JB022539.
- 440 Davidsen, J., Kwiatek, G., Charalampidou, E.-M., Goebel, T., Stanchits, S., Rück,
- 441 M., & Dresen, G. (2017). Triggering processes in rock fracture. *Physical review*
- 442 *letters*, *119*(6), 068501.
- 443 Denlinger, R. P., & RH O'Connell, D. (2020). Evolution of faulting induced by deep
- 444 fluid injection, paradox valley, colorado. *Bulletin of the Seismological Society of*
- 445 *America*, *110*(5), 2308–2327.
- 446 DeVries, P. M., Viégas, F., Wattenberg, M., & Meade, B. J. (2018). Deep learning of
- 447 aftershock patterns following large earthquakes. *Nature*, *560*(7720), 632–634.
- 448 Ellsworth, W. L. (2013). Injection-induced earthquakes. *Science*, *341*(6142).
- 449 Ge, S., & Saar, M. O. (2022). Induced seismicity during geoenery development—a
- 450 hydromechanical perspective. *Journal of Geophysical Research: Solid Earth*,
- 451 *127*(3), e2021JB023141.
- 452 Glasgow, M., Schmandt, B., Wang, R., Zhang, M., Bilek, S. L., & Kiser, E. (2021).
- 453 Raton basin induced seismicity is hosted by networks of short basement faults
- 454 and mimics tectonic earthquake statistics. *Journal of Geophysical Research:*
- 455 *Solid Earth*, *126*(11), e2021JB022839.
- 456 Goebel, T., Rosson, Z., Brodsky, E., & Walter, J. (2019). Aftershock deficiency
- 457 of induced earthquake sequences during rapid mitigation efforts in oklahoma.
- 458 *Earth and Planetary Science Letters*, *522*, 135–143.
- 459 Harr, C. (1988). Final geological well report. *US Bureau of Reclamation Test*
- 460 *Well*(1).
- 461 Hill, R. (2024). *Data and Code for Modeling Paradox Valley Unit [Data Set]*. Zen-
- 462 [odo](https://zenodo.org/record/1388888). Retrieved from [pending](https://zenodo.org/record/1388888)
- 463 Hill, R. G., Weingarten, M., Langenbruch, C., & Fialko, Y. (2024). Mitigation and

- 464 optimization of induced seismicity using physics-based forecasting. *JGR: Solid*
 465 *Earth (in review)*. (in review)
- 466 Ho, T. K. (1998). The random subspace method for constructing decision forests.
 467 *IEEE transactions on pattern analysis and machine intelligence*, *20*(8), 832–
 468 844.
- 469 Ho, T. K., et al. (1995). Proceedings of 3rd international conference on document
 470 analysis and recognition. In *Proceedings of 3rd international conference on doc-*
 471 *ument analysis and recognition*.
- 472 Hsu, Y.-F., Zaliapin, I., & Ben-Zion, Y. (2024). Informative modes of seismicity
 473 in nearest-neighbor earthquake proximities. *Journal of Geophysical Research:*
 474 *Solid Earth*, *129*(3), e2023JB027826.
- 475 Keranen, K. M., & Weingarten, M. (2018). Induced seismicity. *Annual Review of*
 476 *Earth and Planetary Sciences*, *46*, 149–174.
- 477 Keranen, K. M., Weingarten, M., Abers, G. A., Bekins, B. A., & Ge, S. (2014).
 478 Sharp increase in central oklahoma seismicity since 2008 induced by massive
 479 wastewater injection. *Science*, *345*(6195), 448–451.
- 480 King, G. C. P., Stein, R. C., & Lin, J. (1994). Static stress change and the triggering
 481 of earthquakes. *Bull. Seism. Soc. Am.*, *84*, 935–953.
- 482 King, V., & Block, L. (2019, Aug). *Paradox valley seismic and injection data -*
 483 *amerigeoss community platform datahub. (beta)*. Retrieved from [https://](https://urldefense.com/v3/_https://data.amerigeoss.org/dataset/paradox-valley-seismic-and-injection-data_;!Mih3wA!E0xCUAx3ctL8wKS_tp-pNn95UaeXh_lRky7b2Mcg4-S1_-Ss2N0b2nM5ld42UzHIa8rqXmpIaj50ioAx$)
 484 [urldefense.com/v3/_https://data.amerigeoss.org/dataset/paradox](https://urldefense.com/v3/_https://data.amerigeoss.org/dataset/paradox-valley-seismic-and-injection-data_;!Mih3wA!E0xCUAx3ctL8wKS_tp-pNn95UaeXh_lRky7b2Mcg4-S1_-Ss2N0b2nM5ld42UzHIa8rqXmpIaj50ioAx$)
 485 [-valley-seismic-and-injection-data_;!Mih3wA!E0xCUAx3ctL8wKS_tp](https://urldefense.com/v3/_https://data.amerigeoss.org/dataset/paradox-valley-seismic-and-injection-data_;!Mih3wA!E0xCUAx3ctL8wKS_tp-pNn95UaeXh_lRky7b2Mcg4-S1_-Ss2N0b2nM5ld42UzHIa8rqXmpIaj50ioAx$)
 486 [-pNn95UaeXh_lRky7b2Mcg4-S1_-Ss2N0b2nM5ld42UzHIa8rqXmpIaj50ioAx\\$](https://urldefense.com/v3/_https://data.amerigeoss.org/dataset/paradox-valley-seismic-and-injection-data_;!Mih3wA!E0xCUAx3ctL8wKS_tp-pNn95UaeXh_lRky7b2Mcg4-S1_-Ss2N0b2nM5ld42UzHIa8rqXmpIaj50ioAx$)
- 487 King, V. M., Block, L. V., & Wood, C. K. (2016). Pressure/flow modeling and
 488 induced seismicity resulting from two decades of high-pressure deep-well brine
 489 injection, paradox valley, colorado. *Geophysics*, *81*(5), B119–B134.
- 490 Langenbruch, C., Weingarten, M., & Zoback, M. D. (2018). Physics-based forecast-
 491 ing of man-made earthquake hazards in oklahoma and kansas. *Nature commu-*
 492 *nications*, *9*(1), 1–10.
- 493 Levandowski, W., Weingarten, M., & Walsh III, R. (2018). Geomechanical sensi-
 494 tivities of injection-induced earthquakes. *Geophysical Research Letters*, *45*(17),
 495 8958–8965.
- 496 Lin, J., & Stein, R. S. (2004). Stress triggering in thrust and subduction earthquakes

- 497 and stress interaction between the southern san andreas and nearby thrust and
 498 strike-slip faults. *Journal of Geophysical Research: Solid Earth*, 109(B2).
- 499 Lundberg, S. M., & Lee, S.-I. (2017). A unified approach to interpreting model pre-
 500 dictions. *Advances in neural information processing systems*, 30.
- 501 Nikkhoo, M., & Walter, T. R. (2015). Triangular dislocation: an analytical, artefact-
 502 free solution. *Geophysical Journal International*, 201(2), 1119–1141.
- 503 Papazafeiropoulos, G., Muñiz-Calvente, M., & Martínez-Pañeda, E. (2017).
 504 Abaqus2matlab: A suitable tool for finite element post-processing. *Adv. Eng.*
 505 *Softw.*, 105, 9–16.
- 506 Qin, Y., Chen, T., Ma, X., & Chen, X. (2022). Forecasting induced seismicity in ok-
 507 lahoma using machine learning methods. *Scientific Reports*, 12(1), 9319.
- 508 Reasenberg, P. A., & Simpson, R. W. (1992). Response of regional seismicity to
 509 the static stress change produced by the loma prieta earthquake. *Science*,
 510 255(5052), 1687–1690.
- 511 Rice, J. R., & Cleary, M. P. (1976). Some basic stress diffusion solutions
 512 for fluid-saturated elastic porous media with compressible constituents.
 513 *Rev. Geophys.*, 14(2), 227. Retrieved 2021-04-13, from [https://
 514 urldefense.com/v3/_http://doi.wiley.com/10.1029/RG014i002p00227
 515 _";!!Mih3wA!E0xCUax3ctL8wKS_tp-pNn95UaeXh_lRky7b2Mcg4-S1_-
 516 -Ss2N0b2nM5ld42UzHIa8rqXmpIai1FHNQ\\$](https://urldefense.com/v3/_http://doi.wiley.com/10.1029/RG014i002p00227_) doi: 10.1029/RG014i002p00227
- 517 Roeloffs, E., & Denlinger, R. (2009). An axisymmetric coupled flow and deformation
 518 model for pore pressure caused by brine injection in paradox valley, colorado:
 519 Implications for the mechanisms of induced seismicity. *Preliminary Report to*
 520 *the Bureau of Reclamation*.
- 521 Rudnicki, J. W. (1986). Fluid mass sources and point forces in linear elas-
 522 tic diffusive solids. *Mechanics of Materials*, 5(4), 383-393. Retrieved
 523 from [https://
 524 science/article/pii/0167663686900426_";!!Mih3wA!E0xCUax3ctL8wKS_tp
 525 -pNn95UaeXh_lRky7b2Mcg4-S1_-Ss2N0b2nM5ld42UzHIa8rqXmpIahGXh2Vz\\$
 526 doi: \[https://
 527 90042-6_";!!Mih3wA!E0xCUax3ctL8wKS_tp-pNn95UaeXh_lRky7b2Mcg4-S1
 528 _-Ss2N0b2nM5ld42UzHIa8rqXmpIarQvXa1P\\\$\]\(https://urldefense.com/v3/_https://doi.org/10.1016/0167-6636\(86\)90042-6_\)](https://urldefense.com/v3/_https://www.sciencedirect.com/science/article/pii/0167663686900426_)
- 529 Schoenball, M., Davatzes, N. C., & Glen, J. M. (2015). Differentiating induced and

- 530 natural seismicity using space-time-magnitude statistics applied to the coso
531 geothermal field. *Geophysical Research Letters*, 42(15), 6221–6228.
- 532 Segall, P., & Lu, S. (2015). Injection-induced seismicity: Poroelastic and earthquake
533 nucleation effects. *Journal of Geophysical Research: Solid Earth*, 120(7), 5082–
534 5103.
- 535 Shapley, L. S., et al. (1953). A value for n-person games.
- 536 Sharma, S., Hainzl, S., Zöeller, G., & Holschneider, M. (2020). Is coulomb stress the
537 best choice for aftershock forecasting? *Journal of Geophysical Research: Solid*
538 *Earth*, 125(9), e2020JB019553.
- 539 Shirzaei, M., Ellsworth, W. L., Tiampo, K. F., González, P. J., & Manga, M. (2016).
540 Surface uplift and time-dependent seismic hazard due to fluid injection in east-
541 ern texas. *Science*, 353(6306), 1416–1419.
- 542 Stein, R. S. (1999). The role of stress transfer in earthquake occurrence. *Nature*,
543 402(6762), 605–609.
- 544 Stokes, S. M., Ge, S., Brown, M. R., Menezes, E. A., Sheehan, A. F., & Tiampo,
545 K. F. (2023). Pore pressure diffusion and onset of induced seismicity. *Journal*
546 *of Geophysical Research: Solid Earth*, 128(3), e2022JB026012.
- 547 Thompson, B. (2021). *cutde*. Retrieved from [https://github.com/tbenthompson/](https://github.com/tbenthompson/cutde)
548 `cutde`
- 549 Toda, S., Stein, R. S., Richards-Dinger, K., & Bozkurt, S. B. (2005). Forecasting the
550 evolution of seismicity in southern california: Animations built on earthquake
551 stress transfer. *Journal of Geophysical Research: Solid Earth*, 110(B5).
- 552 Townend, J., & Zoback, M. D. (2000). How faulting keeps the crust strong. *Geology*,
553 28(5), 399–402.
- 554 Trugman, D. T., & Ben-Zion, Y. (2023). Coherent spatial variations in the produc-
555 tivity of earthquake sequences in california and nevada. *The Seismic Record*,
556 3(4), 322–331.
- 557 Van Der Elst, N. J., & Brodsky, E. E. (2010). Connecting near-field and far-field
558 earthquake triggering to dynamic strain. *Journal of Geophysical Research:*
559 *Solid Earth*, 115(B7).
- 560 Wang, H. (2000). *Theory of linear poroelasticity: With applications to geomechanics*
561 *and hydrogeology*. Princeton, New Jersey: 287 pp., Princeton Univ. Press.
- 562 Weingarten, M., Ge, S., Godt, J. W., Bekins, B. A., & Rubinstein, J. L. (2015).

- 563 High-rate injection is associated with the increase in us mid-continent seismic-
564 ity. *Science*, 348(6241), 1336–1340.
- 565 Zaliapin, I., & Ben-Zion, Y. (2013). Earthquake clusters in southern california i:
566 Identification and stability. *Journal of Geophysical Research: Solid Earth*,
567 118(6), 2847–2864.
- 568 Zaliapin, I., & Ben-Zion, Y. (2016). Discriminating characteristics of tectonic and
569 human-induced seismicity. *Bulletin of the Seismological Society of America*,
570 106(3), 846–859.
- 571 Zaliapin, I., Gabrielov, A., Keilis-Borok, V., & Wong, H. (2008). Clustering anal-
572 ysis of seismicity and aftershock identification. *Physical review letters*, 101(1),
573 018501.

8 Supplementary

8.1 Model Pre-processing

A variety of issues and subsequent solutions arose in the model preprocessing that is important to elaborate on. As mentioned, previous work already compiled resources into a comprehensive, fully coupled poroelastic model of the PVU (Denlinger & RH O’Connell, 2020). However, this model was not easily portable to Abaqus and lacked sufficient discretization to capture large pressure gradients near the well. The methodology used to transfigure the initial model are presented here. We compare the model to a well known analytical solution and observed wellhead pressures to confirm its robustness.

8.1.1 Material Parameters and Meshing

The first difficulty with the Denlinger and O’Connell (D&O) model (Denlinger & RH O’Connell, 2020) is that the poroelastic material parameters are all defined at the nodes of the mesh. In Abaqus, there are a few material parameters defined at the nodes (pore pressure, void ratio, and saturation), but the elements (hexahedrons defined spatially by 8 nodes) are assigned other material parameters (ie. Young’s modulus and bulk modulus of solid grains). After simple conversions of the given material parameters in the D&O model to the values used in Abaqus, we thought the best way to solve the issue of defining the *node only* values to elements would be to average the 8 nodal coordinates that make up a hexahedron element to the value at that element.

However, the averaging proved ineffective for a variety of reasons. First, the D&O model near the region of the well head experiences strong changes in material values. The Leadville formation, the high permeable injection formation, is embedded in low permeable material. The nodal change between these materials was actually only 1 node thick in some instances so by taking the average of 8 nodes resulted in significantly reducing the order of magnitude of material permeability for areas near fluid injection. Second, the strong changes in material values coupled with the large spatial discretization of the D&O model near the wellhead resulted in unrealistic gradients and convergence issues.

Therefore, in order to solve the issues present with the conversion of the D&O model to Abaqus, we decided to make several adjustments to our model that we believe make it a stronger model overall. First, we decided to reduce the spatial discretization near

604 the well head. The well head is actually composed of 3 separate perforated injection zones
605 and creates strong pressure gradients that require smaller spatial sampling in order to
606 capture the large and rapid changes there. This is difficult to do based on the previous
607 mesh since preserving spatial features such as dipping beds and down scaling material
608 features is not straight forward. Thankfully, the vertical discretization was already well
609 defined by the D&O model so the only change to the discretization was the horizontal
610 directions. We solved this problem by preserving the number of elements whilst chang-
611 ing the horizontal spacing to grow exponentially from the location of the well head. Then,
612 the vertical spacing and material parameters of the D&O model are preserved in the smaller
613 spacing by using a nearest point search measured in Euclidean distance. The spatial mesh-
614 ing changes between the D&O model and ours are shown in Figure 1.

615 The second adjustment we made was in the determination of material parameters
616 throughout the model. As previously mentioned the D&O model allows for entirely unique
617 material parameters at every node, which caused difficulties in convergence for Abaqus.
618 Using the newly discretized mesh of nodes/elements, and their associated material pa-
619 rameters, we applied a k-medoids clustering algorithm to cluster the nodes/elements based
620 on similar material metrics across the combined set of materials. K-medoids is similar
621 to k-means clustering, but instead of choosing the average from the kth cluster it chooses
622 an actual data point as the center of the cluster. We worked with several different ma-
623 terial cluster values, but ultimately decided on 1000. At this number, the model preserves
624 many of the naturally occurring geological features such as the layered beds and salt domes
625 whilst also maintaining a high level of material contrast near the wellhead without gen-
626 erating drastic gradients.

627 ***8.1.2 FEM Results Compared to Analytical Solution/Observation***

628 A well known analytical solution exists to describe the spatial and temporal evo-
629 lution of pore pressure due to continuous fluid injection into a poroelastic full space (Rudnicki,
630 1986). In order to gauge the success of the model, we first compare this solution to the
631 3D model using homogeneous material parameters. Additionally, we reduce the 3 injec-
632 tion nodes to a single node to better reflect the analytical solution. The radial analyt-
633 ical solution of pore pressure is compared with the closest radial axis given by the nodes
634 shown in Figure 22. The solution for pore pressure matches well to the analytical solu-

635 tion after 10 days of constant injection using a typical bulk value of the crust as shown
636 in Figure 23.

637 One thing to note is that the solution of pore pressure increases rapidly closer to
638 the point of injection. The strong pressure gradients at this location require smaller el-
639 ements than the horizontal discretization in the D&O model (200 m).

640 With the model now confirmed in the simplest case it was time to test a variety
641 of k-medoid models, as previously described, and compare them to the observed well-
642 head pressures to confirm that the model was capable of capturing the observations. It
643 is important to note that any complex model will result in overfitting of the wellhead
644 data, and thus poor predictive ability for future data.

645 There has been a plethora of previous work from observational drilling to pressure-
646 flow modeling designed to capture the reservoir permeability structure (V. King & Block,
647 2019). These different observations and modeling have provided a sizeable range of per-
648 meability values. For example, the permeability of intact limestone and dolomite varies
649 from 0.01 to 0.1 mD (Bear, 1988). Fracturing is expected to increase permeability out-
650 side of this laboratory setting. Drill stem tests gave an original permeability of 7.97 mD,
651 yet at the same time additional analysis indicated permeability between 1.3 and 1.5 mD.
652 Samples from a well 4.6 km to the northeast yielded permeability ranges of 0.03 to 1.3
653 mD (Harr, 1988). An earlier model by Denlinger and Roeloffs (Roeloffs & Denlinger, 2009)
654 arrived at a permeability in the injection zone of 28 mD, with significantly lower values
655 for the other formations. Additional pressure-flow models also arrive at ranges of 9.06
656 to 29.2 mD for certain injection phases (V. King & Block, 2019). The current *best* model
657 (the D&O model) throughout the entire model domain, only has a maximum permeabil-
658 ity of 1.97 mD. The final 1000 k-medoids model, modeled at constant injection rate (typ-
659 ical daily average from PVU injection data), is compared with several hypothetical an-
660 alytical solutions for constant injection rate for a range of bulk permeabilities in Figure
661 24.

662 The final 3D heterogeneous model compares well with a range of typical observa-
663 tional values and observed wellhead pressures. In the near-field, the permeability matches
664 the higher permeability analytical solutions as expected since there is likely fractured
665 media in this location (V. King & Block, 2019). In the far-field, where the permeabil-
666 ity structure is expected to decrease, the model approaches the lower permeability an-

667 analytical solution. For the future, it will likely be important to test a variety of physics
668 based models to understand the sensitivity introduced in the machine learning. How-
669 ever, we are confident in the evidence presented that our current model, adopted from
670 the D&O model, is robust enough to continue with the primary goal of this work.

8.2 Supplementary Figures

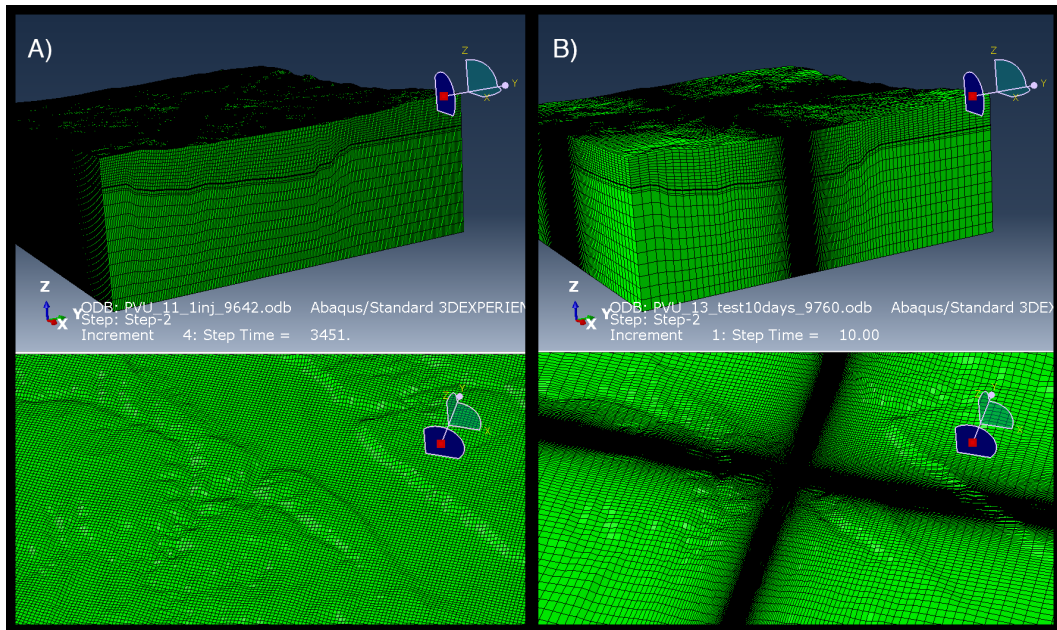


Figure 1. Previous model mesh from D&O model (Panel A) with surface view of well location compared to (Panel B) our smaller discretized model with similar surface view.

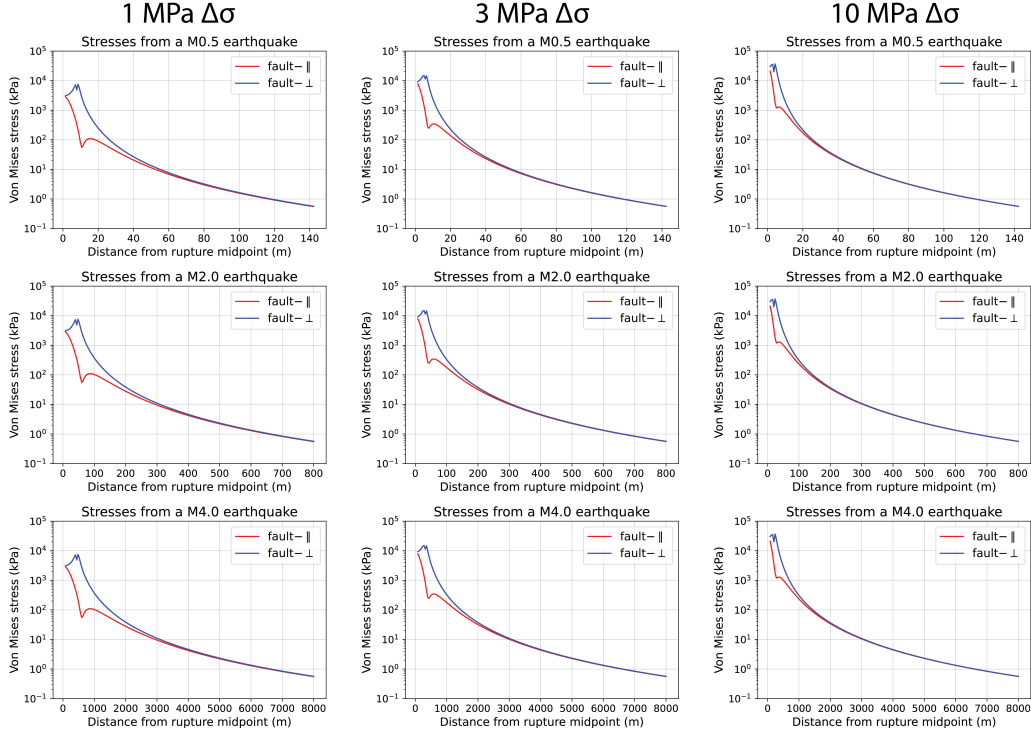


Figure 2. The von Mises stress in kPa for the three varying earthquake magnitudes (0.5, 2.0, and 4.0) for three varying stress drops (1, 3, and 10 MPa). We use cutde (Thompson, 2021) to resolve stress transfer produced from fullspace triangle dislocation elements assuming a uniform stress drop, a shear modulus of 30 GPa, and a Poisson ratio of 0.25. We show that the von Mises stress is self similar for opposite receiver planes at certain distances, dependent on the magnitude, produced by the dislocation. We use the triggering threshold of 10 kPa (Reasenberg & Simpson, 1992; Stein, 1999) which increases depending on the magnitude size. This distance is our perturbable radius used for the earthquake feature.

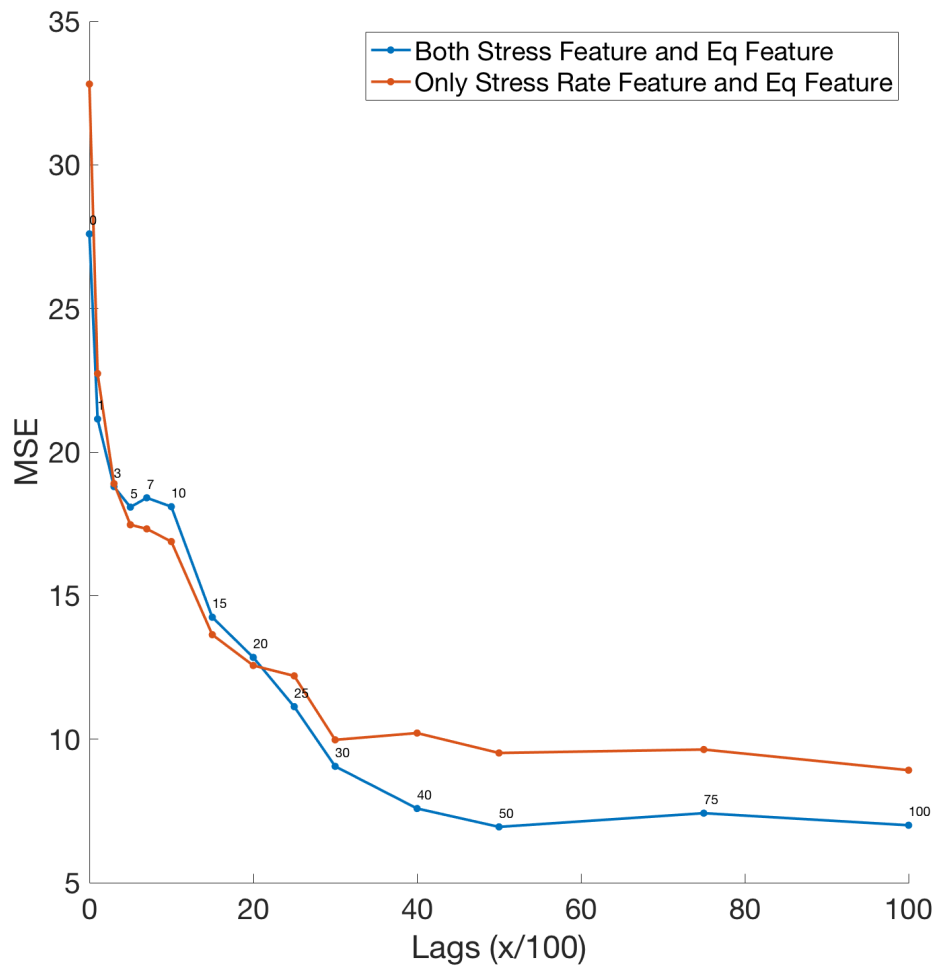


Figure 3. A sensitivity test to increasing and the overall MSE fit to the seismicity rate. We find that there is a local minimum near 5 lags. The fit does not improve after approximately 50 lags.

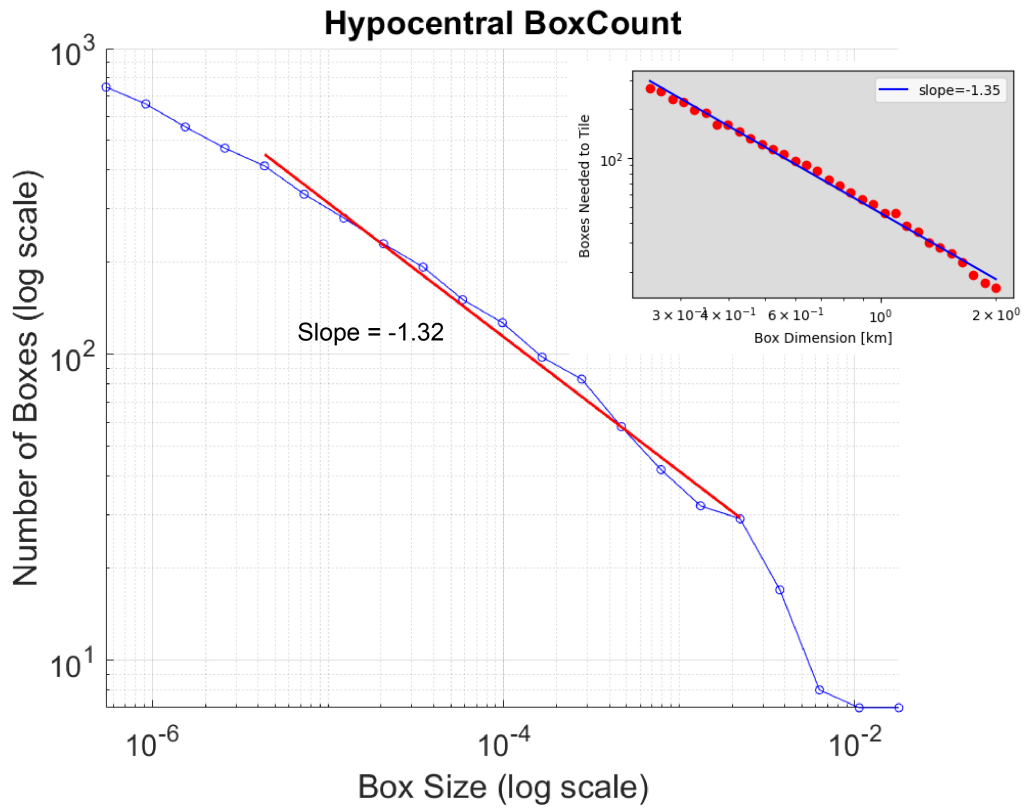


Figure 4. Hypocentral and epicentral (inlet) box-counting procedures with good agreement on the fractal dimension $d_f=1.32$ of the earthquakes at Paradox Valley.

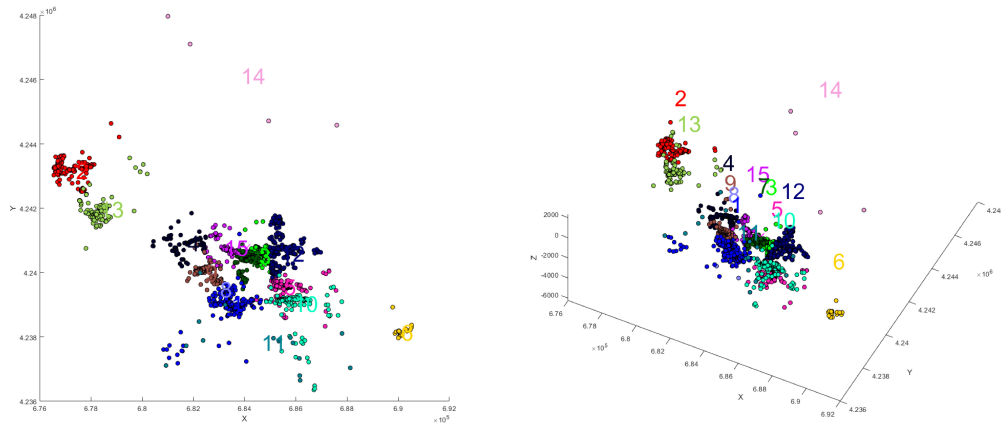


Figure 5. Different k-means cluster locations (1-15) of seismicity for the PVU. We extract the pore pressure at the center of each seismicity cluster from the numerical model in the subsequent figures. We include results for the near well cluster (7), two further regions with more diffuse responses (4) and (10) as well as farther distance (2) and (6).

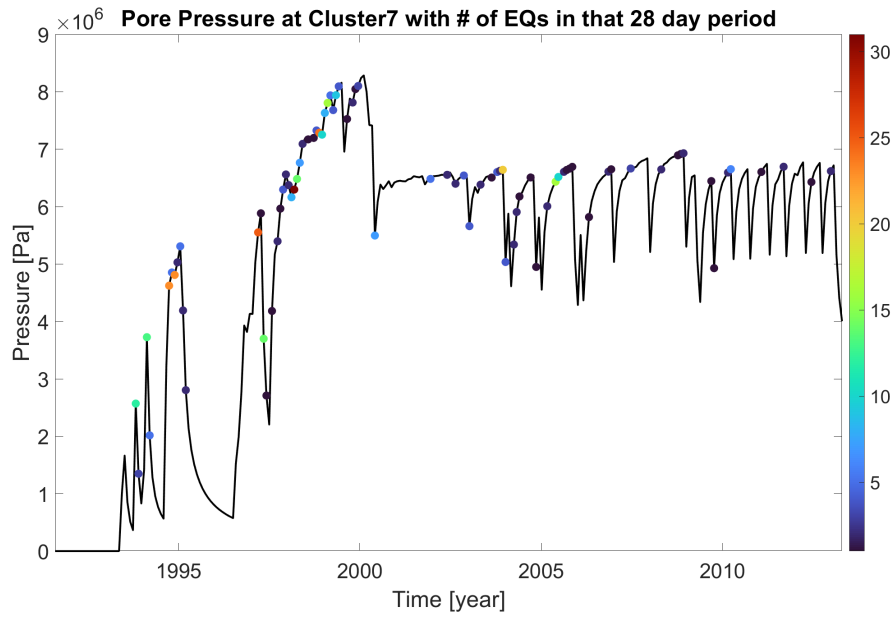


Figure 6. Cluster 7 near the well and pore pressure profile at the center of cluster. The pore pressure mimics the injection well rates due its close vicinity to the well.

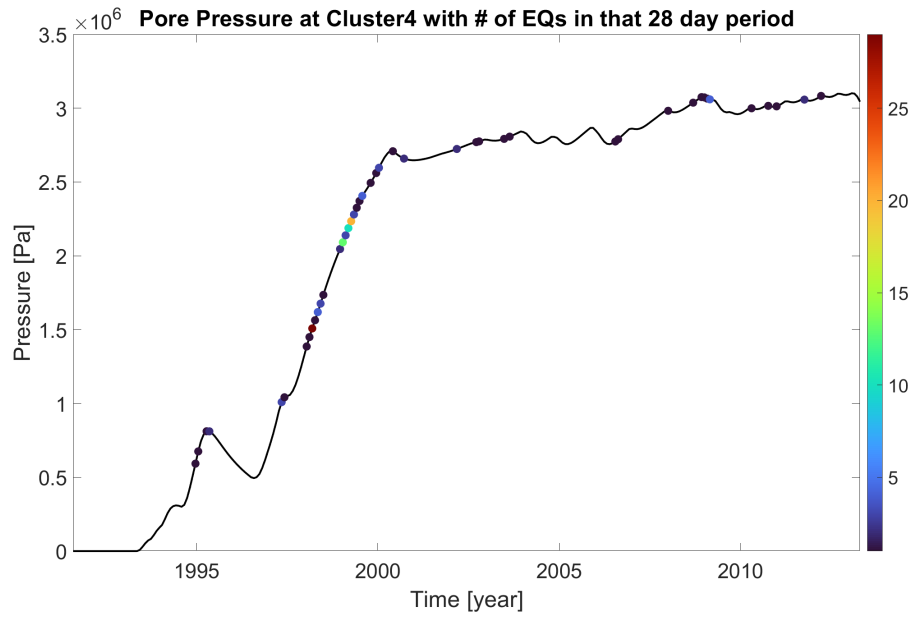


Figure 7. Cluster 4.

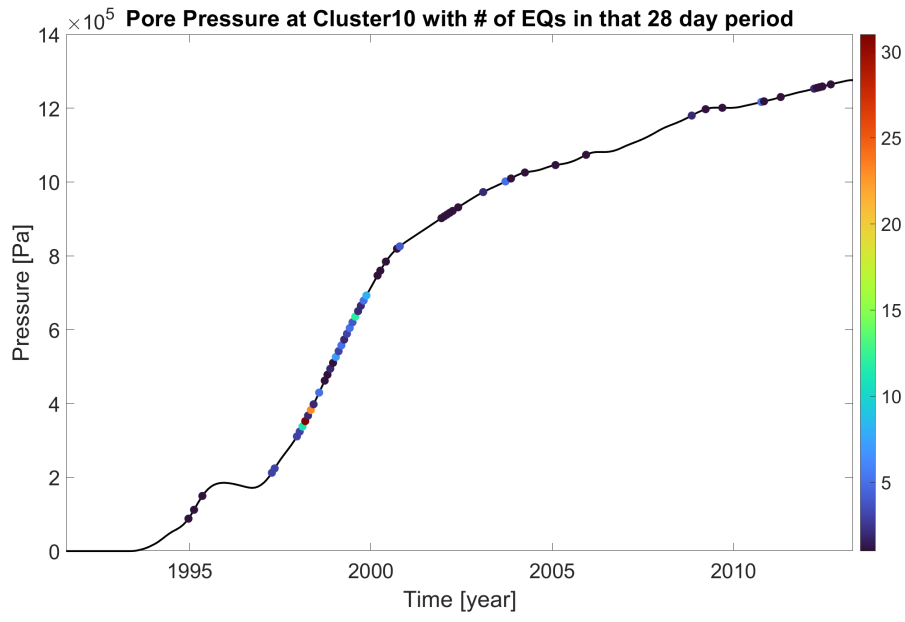


Figure 8. Cluster 10.

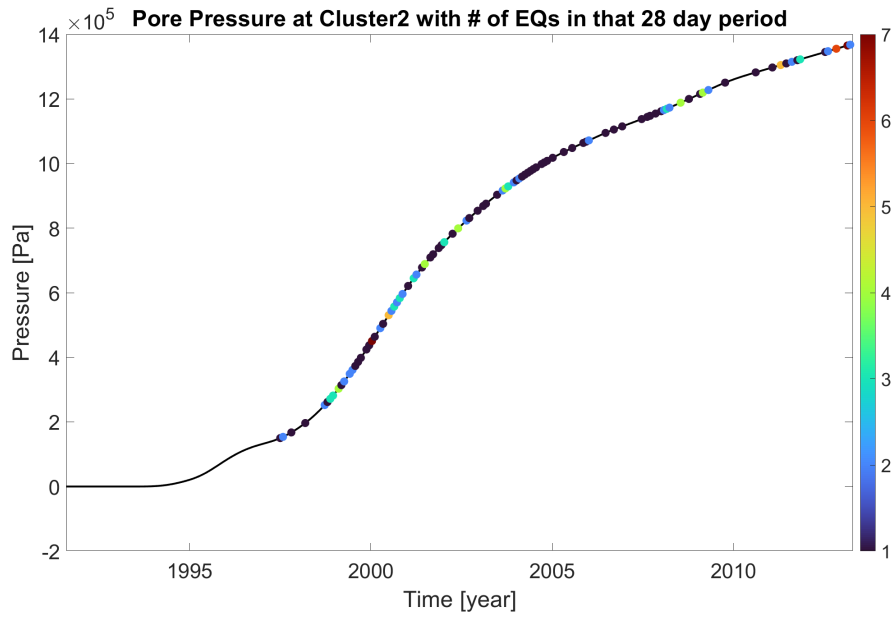


Figure 9. Cluster 2.

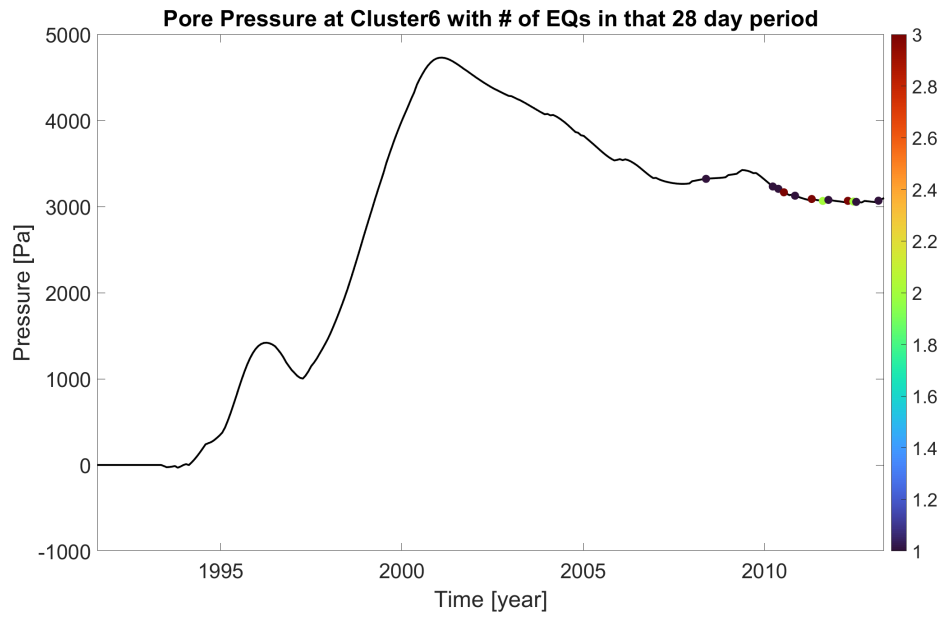


Figure 10. Cluster 6.

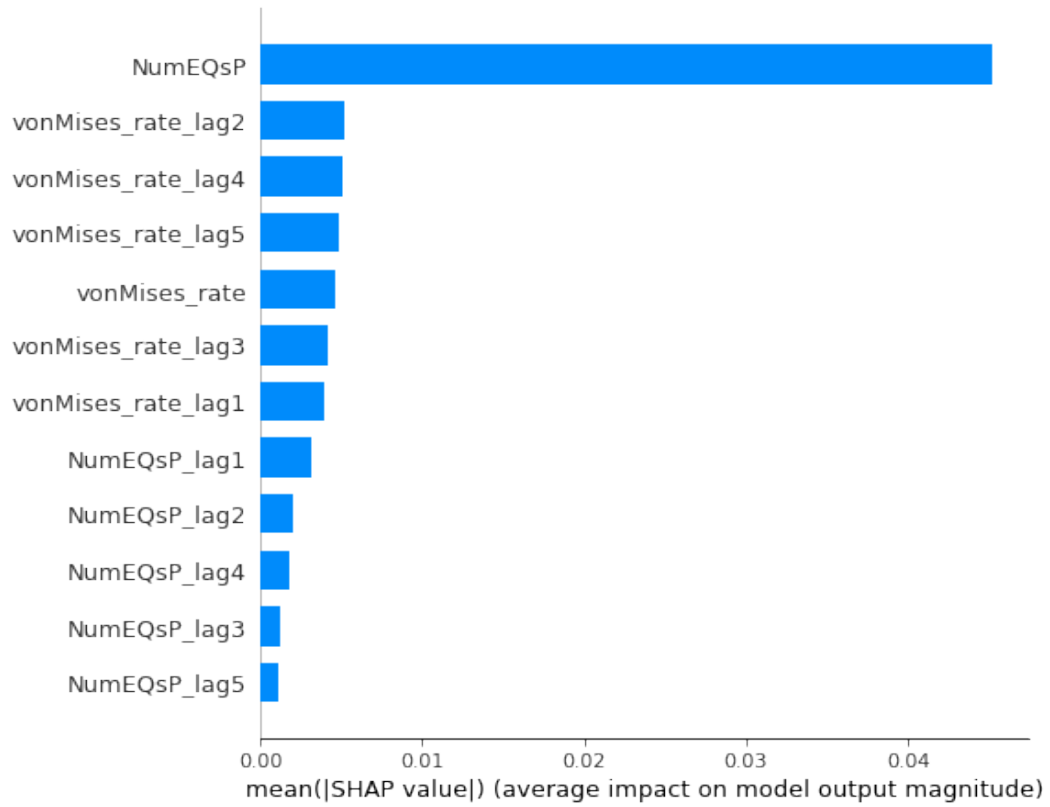


Figure 11. Similar to SM Figure 15 but for the model that includes both the von Mises stress and the von Mises stress rate. This represents 2927 total events. The most important feature is the number of perturbable earthquakes (NumEQsP) that occurred during that same time step as the earthquake in question. The next 65 variables are a mix of the von Mises and von Mises rate.

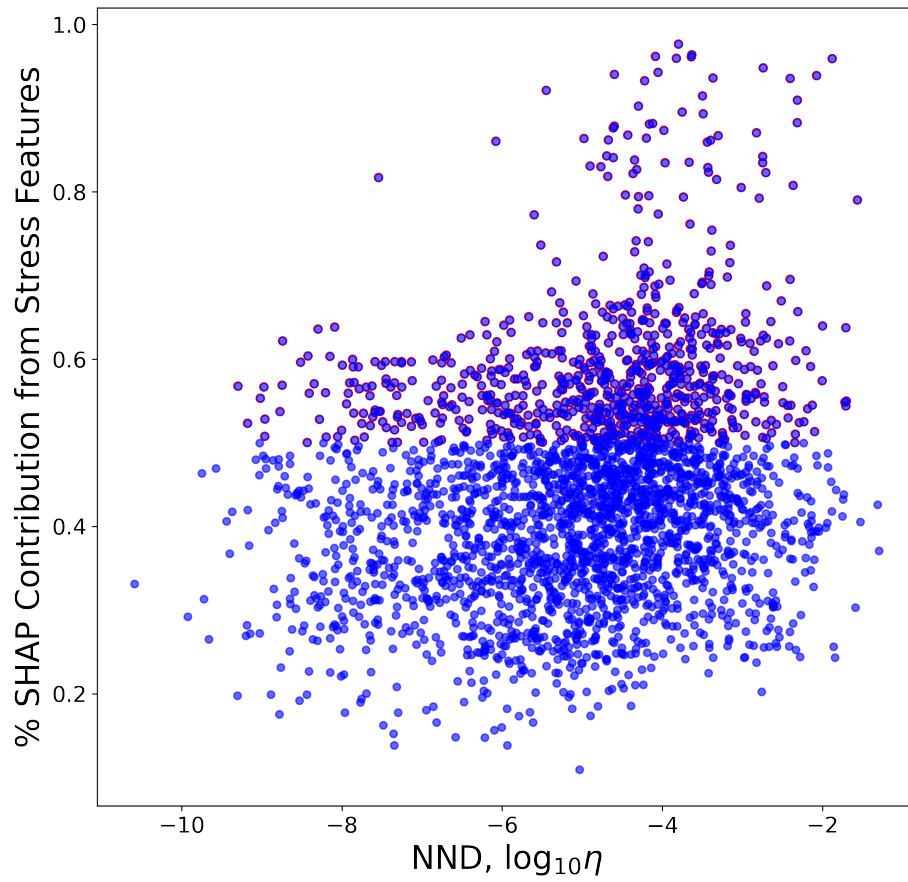


Figure 12. Similar to Figure 3c but for the model that includes both the von Mises stress and the von Mises stress rate. There is more earthquakes associated with the clustered mode, but still a large amount of background mode earthquakes.

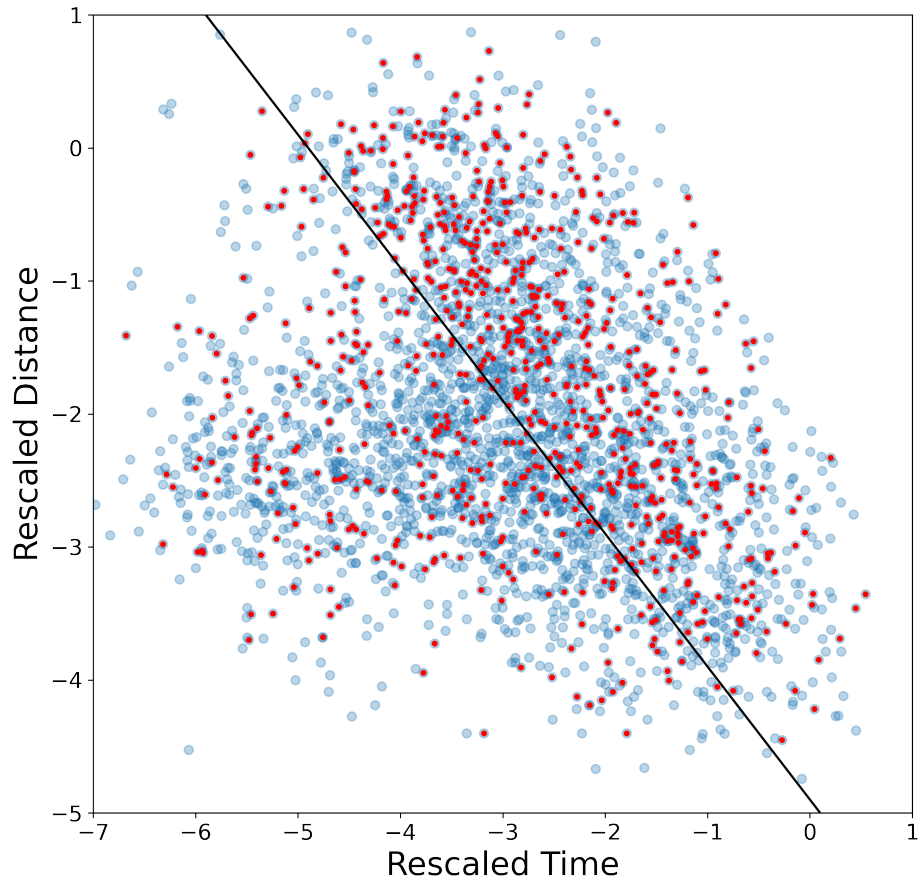


Figure 13. Similar to Figure 3b but for the model that includes both the von Mises stress and the von Mises stress rate. There is more earthquakes associated with the clustered mode, but still a large amount of background mode earthquakes.

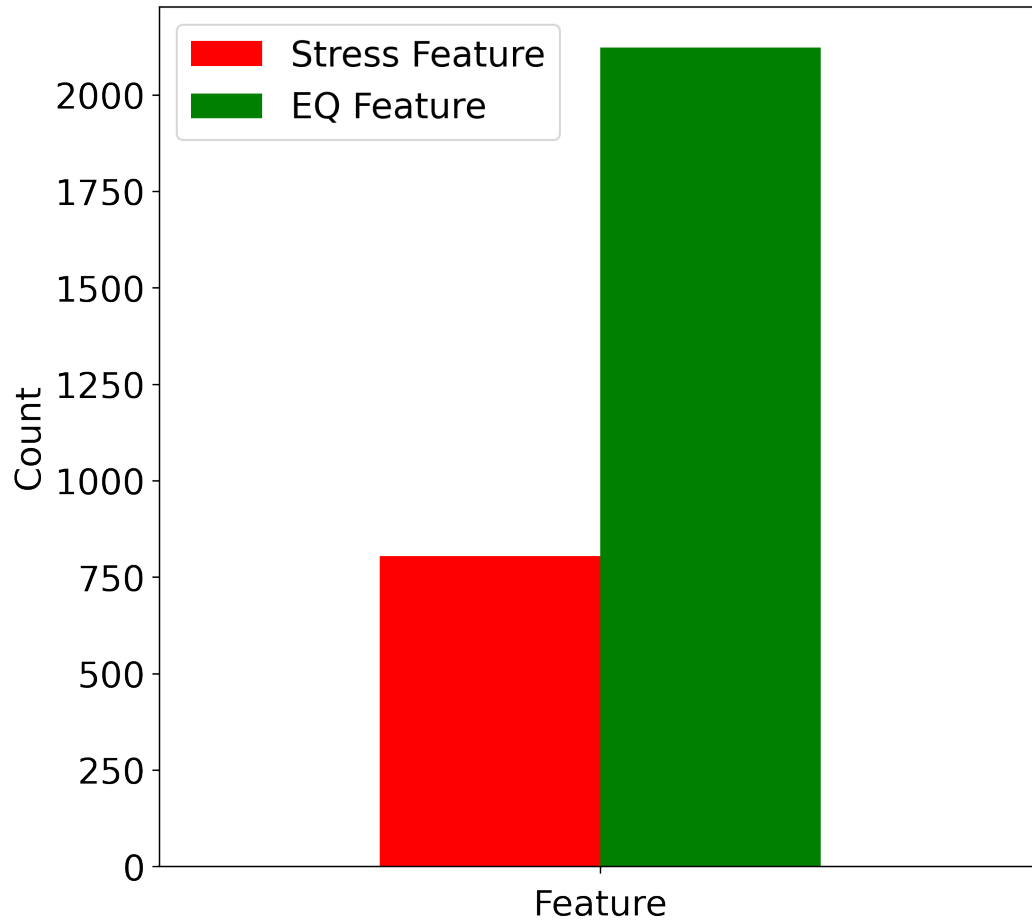


Figure 14. Similar to Figure 4e but for the model that includes both the von Mises stress and the von Mises stress rate. Ratio of the earthquake stress contribution totals for both the stress features and the earthquake features. For our model of including +5lags the stress feature to earthquake feature ratio approximately 1:3 which is must higher than the (1:5) ratio seen in the model that only has one stress feature.

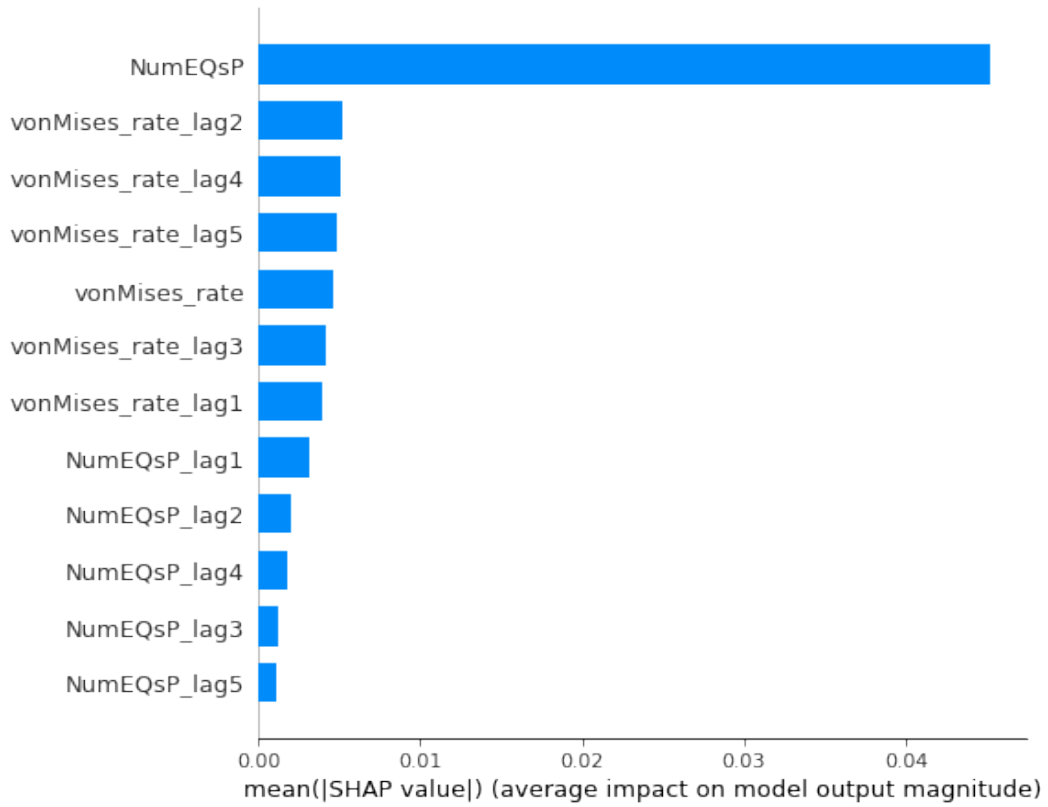


Figure 15. Mean absolute SHAP value for times in the model that an earthquake actually occurred. This represents 2927 total events. The most important feature is the number of perturbable earthquakes (NumEQsP) that occurred during that same time step as the earthquake in question. The next 6 variables are all the stress rate from the stress change from the injection.

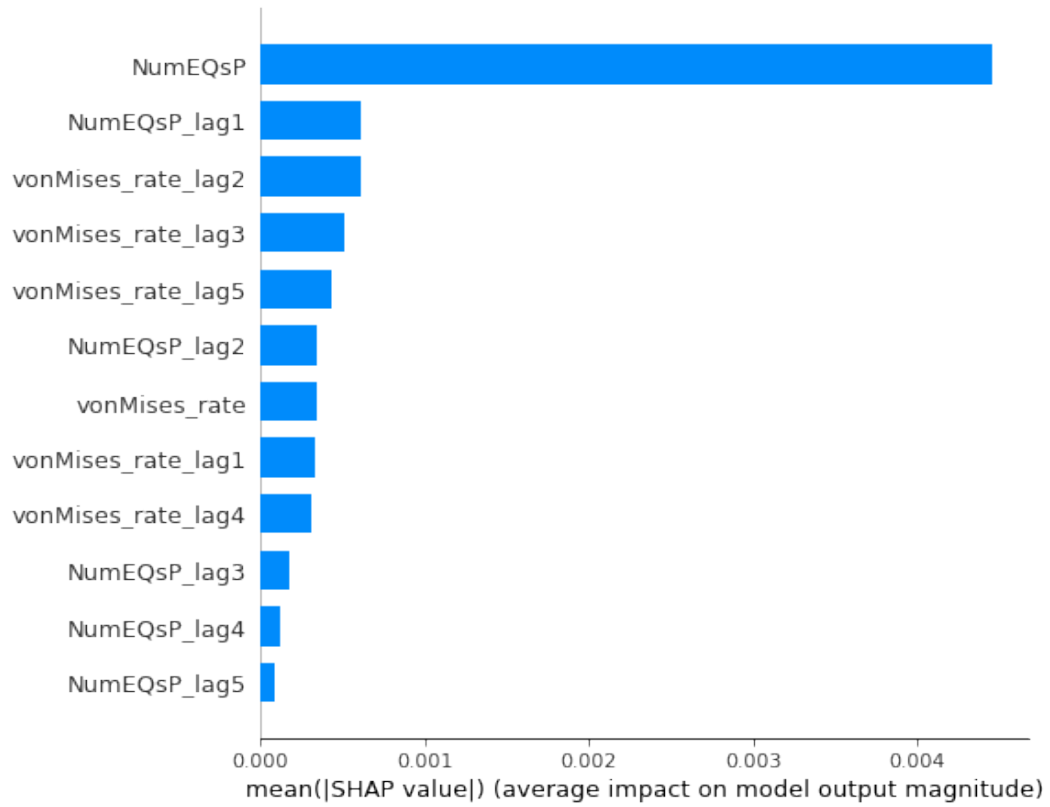


Figure 16. Similar to SM Figure 15 except for all time steps in the model which includes the time steps when an earthquake is not occurring ($2927 * 284 = 831,268$ total samples).

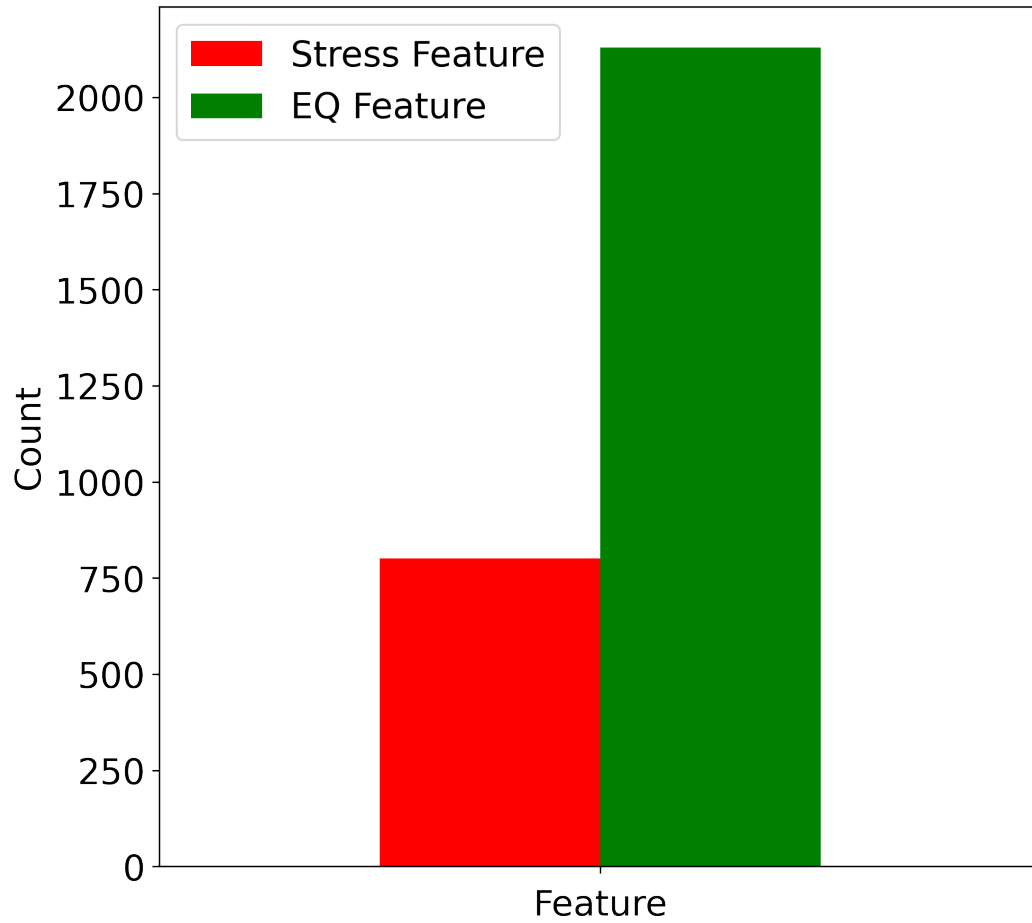


Figure 17. Similar to SM Figure 14 but for the model that includes both the von Mises stress and the von Mises stress rate and only +3 lags. The ratio is (0.3762) compared with the ratio at +5 lags (0.3789). Implying, that the ratio is not sensitive to increasing lags after +3.

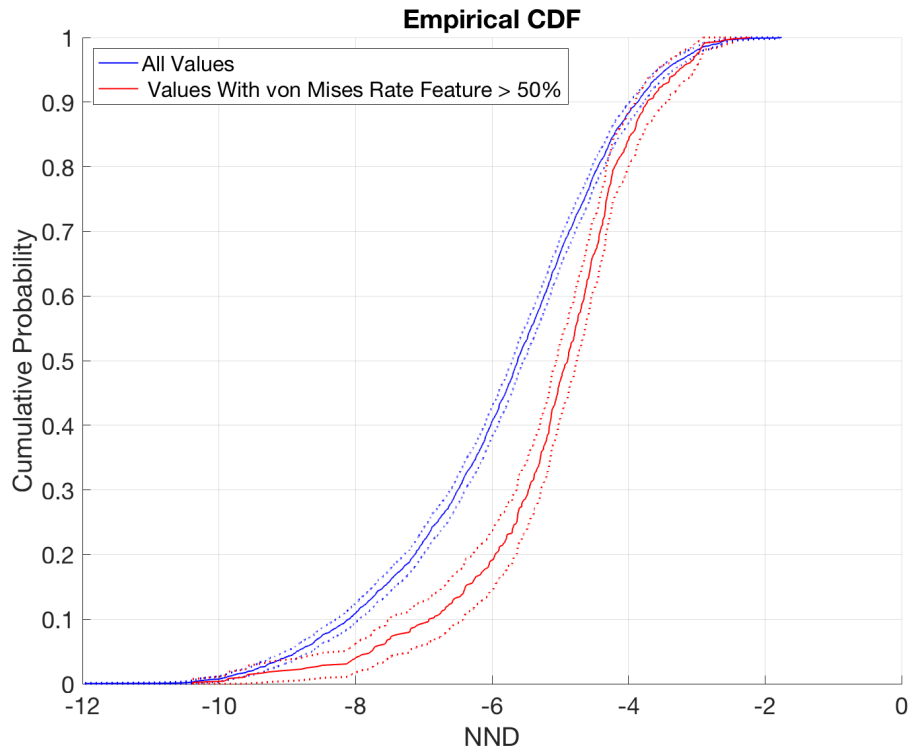


Figure 18. Empirical cumulative density functions of the two sample Kolmogorov–Smirnov test. We show that the distribution for the earthquakes with stress contribution $>50\%$ are not drawn from the same distribution as the total earthquakes with 99% confidence. Dashed line represents lower and upper confidence bounds for each distribution.

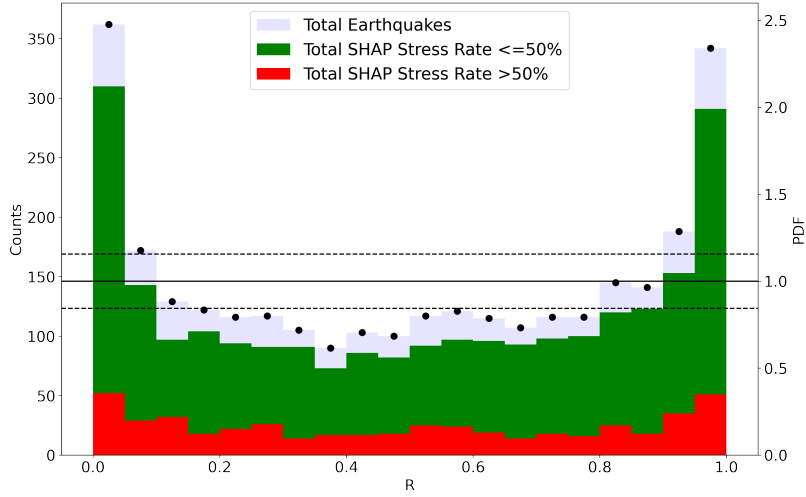


Figure 19. Results of interevent time measure R -test (Van Der Elst & Brodsky, 2010; David-
 sen et al., 2017). The histograms represent count of earthquakes for the total earthquakes (blue)
 and the portion of this set for the the earthquake-driven earthquakes (green) and injection-driven
 earthquakes (red). The overall events reject the null-hypothesis due to the PDF of the interevent
 time ratio R existing outside the the dotted lines corresponding to the 95% confidence inter-
 vals of a Poisson process. Notice that the bimodal tails near $R = 0$ and $R = 1$ are indicative
 of clustering. The majority of the these tails are composed of earthquake-driven events. The
 injection-driven earthquakes are considerably flatter and represent a lower portion of the clus-
 tered seismicity in the overall catalog.

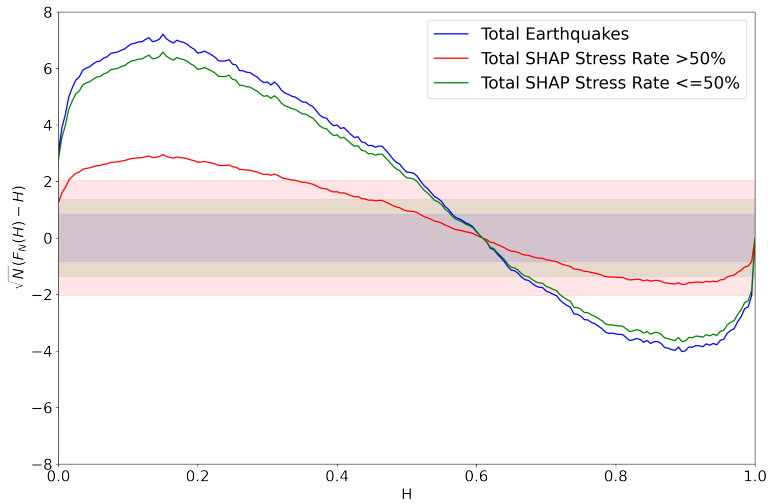


Figure 20. Results of the two sample Kolmogorov-Smirnov test for the distribution of the H statistics obtained by the Bi-test (Bi et al., 1989; Baró et al., 2014; Davidsen et al., 2021). The overall seismicity (blue) and the portion of cumulative components of the earthquake-driven earthquakes (green) and injection-driven earthquakes (red). The three color bars represent the 50%, 95%, and 99.95% confidence bounds for the null hypothesis of a Poisson process ($F_n(H) = H$). Notice that the portion H attributed to injection-driven earthquakes are significantly flatter compared to the clustered earthquake-driven earthquakes which implies a smaller component of the clustered seismicity albeit we can not reject that it is clustered.

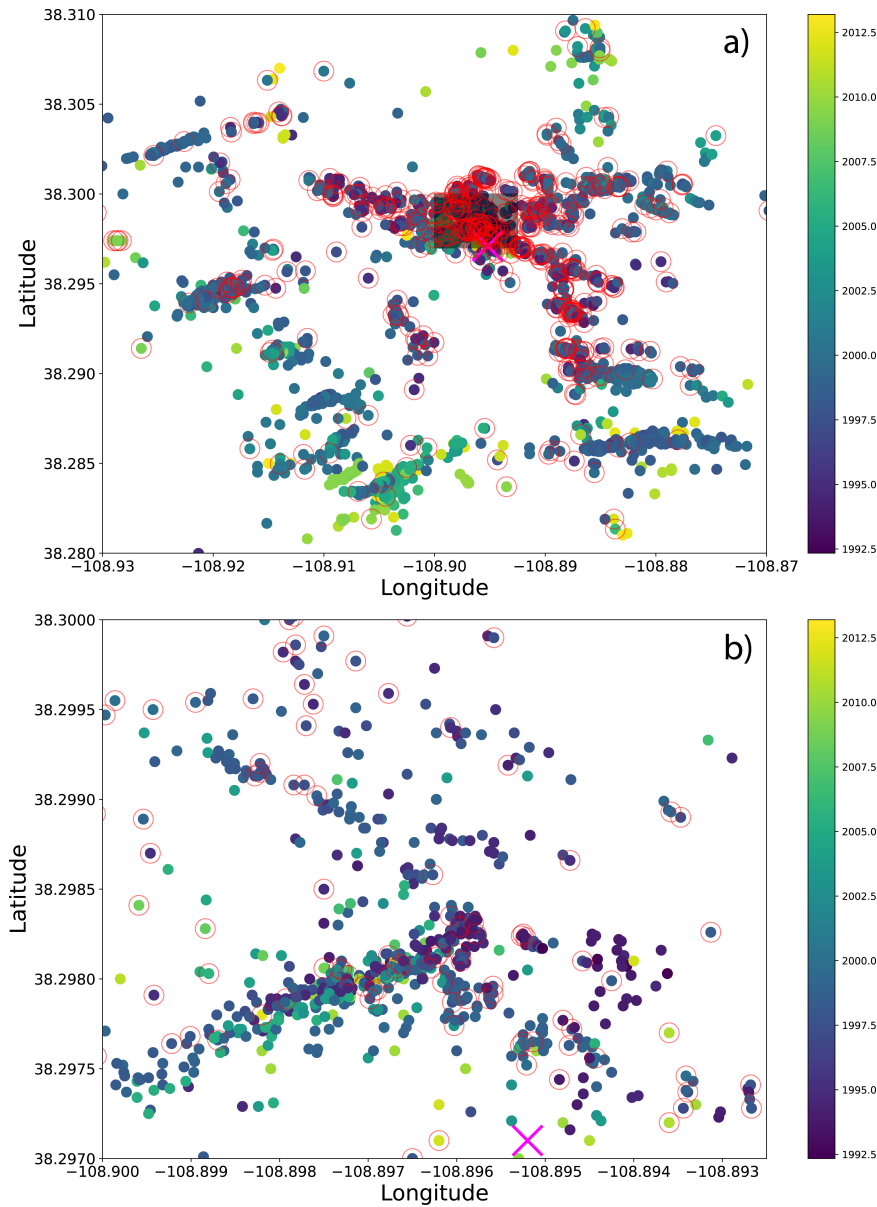


Figure 21. a) Map view of most earthquakes used in our study and denoted in color by the time they occurred. The red circled events represent those circled in red in Figure 3 (i.e. earthquakes that had $>50\%$ stress feature contribution). b) same as above panel, but zoomed in near well. The earthquakes strongly stress driven near the injection well, but also appear at different clusters throughout the domain. Often those away from the well have early times compared to the other earthquakes in their cluster suggesting they may be starting the seismicity in those areas. There are some examples of earthquakes that are close but nearly stress driven as opposed to earthquake driven as well.

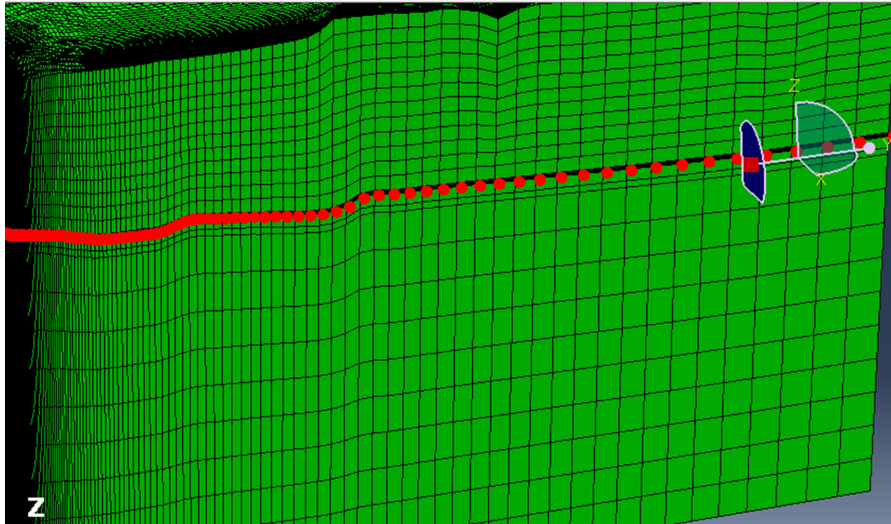


Figure 22. Nodes used in comparison with analytical solution. Well is located on the left and extends to the far field on the right.

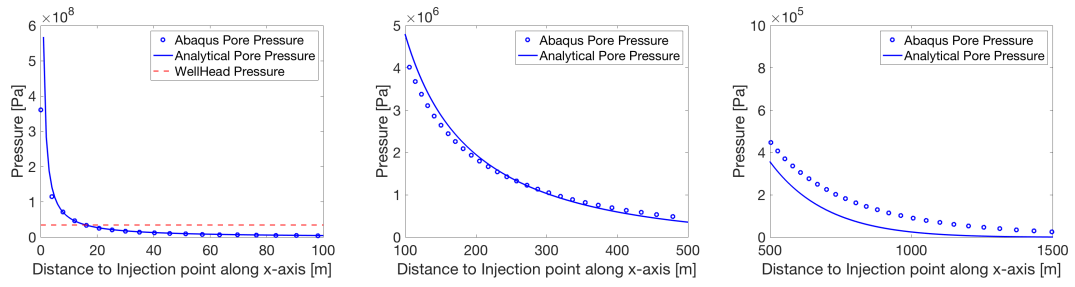


Figure 23. Analytical solution compared to the homogeneous 3D model. Dashed red line represents the average well head pressure of the observed PVU.

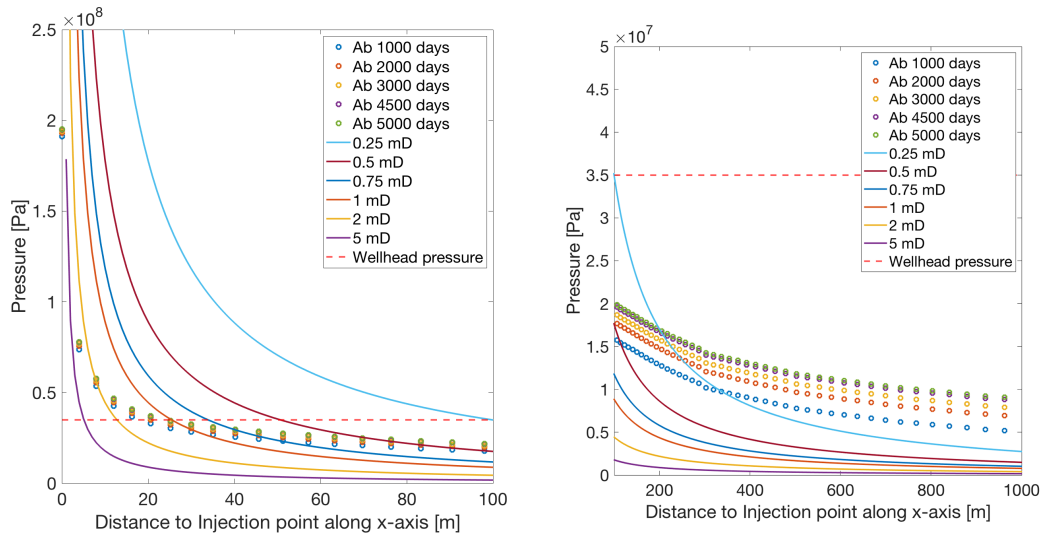


Figure 24. Final 1000 k-medoids model compared to several analytical solutions for a variety of constant rate injection times.